LIMNOLOGY
and
OCEANOGRAPHY: METHODS

Limnol. Oceanogr.: Methods 9, 2011, 396–425

Intercomparison of shallow water bathymetry, hydro-optics, and benthos mapping techniques in Australian and Caribbean coastal environments

Arnold G. Dekker[1,2], Stuart R. Phinn[2]*, Janet Anstee [1], Paul Bissett[3], Vittorio E. Brando[1,2], Brandon Casey[4], Peter Fearns[6], John Hedley[7,8], Wojciech Klonowski[6], Zhong P. Lee[5], Merv Lynch[6], Mitchell Lyons[2], Curtis Mobley[9], and Chris Roelfsema[2]*

1. Environmental Earth Observation Group, Division of Land and Water, CSIRO, Canberra, Australia, 2601
2. Centre for Spatial Environmental Research, School of Geography, Planning and Environmental Management, The University of Queensland, Brisbane, Queensland, Australia, 4072
3. Florida Environmental Research Institute
4. QinetiQ North America, Stennis Space Center, MS 39529
5. Geosystems Research Institute, Mississippi State University, Stennis Space Center, MS 39529
6. Department of Imaging and Applied Physics, Curtin University, Perth, Western Australia, Australia, 6845
7. School of Biosciences, University of Exeter, Exeter, EX4 4PS, UK
8. ARGANS Ltd, UK
9. Sequoia Scientific Inc, 2700 Richards Road, Suite 107, Bellevue, Washington, 98005 USA

Abstract

Science, resource management, and defense need algorithms capable of using airborne or satellite imagery to accurately map bathymetry, water quality, and substrate composition in optically shallow waters. Although a variety of inversion algorithms are available, there has been limited assessment of performance and no work has been published comparing their accuracy and efficiency. This paper compares the absolute and relative accuracies and computational efficiencies of one empirical and five radiative-transfer-based published approaches applied to coastal sites at Lee Stocking Island in the Bahamas and Moreton Bay in eastern Australia. These sites have published airborne hyperspectral data and field data. The assessment showed that (1) radiative-transfer–based methods were more accurate than the empirical approach for bathymetric retrieval, and the accuracies and processing times were inversely related to the complexity of the models used; (2) all inversion methods provided moderately accurate retrievals of bathymetry, water column inherent optical properties, and benthic reflectance in waters less than 13 m deep with homogeneous to heterogeneous benthic/substrate covers; (3) slightly higher accuracy retrievals were obtained from locally parameterized methods; and (4) no method compared here can be considered optimal for all situations. The results provide a guide to the conditions where each approach may be used (available image and field data and processing capability). A re-analysis of these same or additional sites with satellite hyperspectral data with lower spatial and radiometric resolution, but higher temporal resolution would be instructive to establish guidelines for repeatable regional to global scale shallow water mapping approaches.

*Corresponding joint first authors: E-mail: arnold.dekker@csiro.au and s.phinn@uq.edu.au

Acknowledgments

The workshops that resulted in this paper were funded by an Australian Research Council (ARC) International Linkage Grant (LP) to S. Phinn, United States Office of Naval Research (ONR) Funds, Australia's Commonwealth Scientific and Research Organisation (CSIRO), and the University of Queensland. Dr. Joan Cleveland (ONR) also provided support funds. The data sets used in this work were produced from two previously funded large scale international collaborative research projects: (1) Moreton Bay work was funded through an ARC Linkage Grant to J. Marshall and S. Phinn at the University of Queensland and a Cooperative Research Centre grant to S. Phinn and A. Dekker; and (2) Lee Stocking Island work was funded through ONR as part of the Coastal Benthic Optical Properties (COBOP) accelerated research initiative. C. Mobley and Z. Lee received support from ONR. A special thanks to the PHILLS project team at the Naval Research Laboratory. A number of other scientists were involved in earlier discussions to design this project: Prof. Peter Mumby, Dr. Steve Ackleson, and Dr. Curt Davis. Rebecca Edwards at CSIRO provided editorial and formatting assistance.

DOI 10:4319/lom.2011.9.396

Optically shallow waters, those where the bottom is visible from the water surface and measurably influences the water-leaving radiance, include inland waters through to estuarine and tropical coral reef and temperate coastal ecosystems. Over

optically deep waters, there is no measurable water leaving radiance signal from the substratum. Mapping these optically shallow environments provides essential information in the form of maps of bathymetry, water quality and bottom properties, as needed for science, resource management, and defense operations (Green et al. 2000; Phinn et al. 2005). Remote sensing offers a practical means of regularly mapping and monitoring these environments and parameters at spatial and temporal scales applicable to science, resource management, and defense activities. A number of methods currently exist to map bathymetry, water quality, and benthic/substrate composition and their properties from remotely sensed data. However, there is no guidance on which method is most appropriate or accurate for the range of conditions encountered in optically shallow waters This work adds significantly to the IOCCG (2006) evaluation of IOP retrieval algorithms by demonstrating relative performance for bathymetric and bottom reflectance in addition to IOP retrieval.

The potential to estimate water column depth, constituents of the water column, and benthic cover types over large areas and/or in remote locations from remote sensing data have been discussed for over two decades, with significant attention paid to empirical approaches (Clark et al. 1987; Lyzenga 1981; Philpot 1989) that may be location- or data-limited (Lee et al. 2001; Stumpf 1987). Semi-analytical and radiative transfer–based forward models and semi-analytical (SA) or look-up table based spectrum matching (LUT) inverse-models have several advantages for mapping shallow water environments, presuming that a remote sensing image has already been corrected for atmospheric and air/water interface effects (Dekker et al. 2007):

1. Repeatability: the method can be applied to multi-temporal images and corrections for changing water column depth (tides) and varying concentrations of water column constituents is possible;
2. Transferability: application of the models to data from a variety of imaging sensors is straightforward;
3. Sensitivity and error analysis can be objectively determined; and
4. new knowledge can be added to the simulations and can be retrospectively applied to remote sensing images and archives(e.g., global Landsat Thematic Mapper data archive from 1984 onwards).

The following is a brief summary of the developments in this area. Lee et al. (1999) first developed a semi-analytical model for shallow water remote sensing based on radiative transfer. Lee et al. (2001) used an inversion optimization approach to simultaneously derive water depth and water column properties from hyper-spectral data in coastal waters. Adler-Golden et al. (2005) present an algorithm similar to that of Lee et al. (2001). However, it makes the simplifying assumption of constant water optical properties within the scene. Mcintyre et al. (2006) presented an application of the (Lee et al. 2001) inversion modeling approach to clear waters that included a quantitative comparison of model-derived depth with high resolution multi-beam acoustic bathymetry data. Several authors recently extended the method developed by Lee et al. (1999) and Lee et al. (2001) by incorporating linear unmixing of the benthic cover. Giardino et al. (2007) used two substrate classes (bare sand and submerged macrophytes) for the littoral zone of a lake, whereas Goodman and Ustin (2007) and Klonowski et al. (2007) integrated a semi-analytical inversion model with a linear unmixing of three substratum types for coral reef environments. A different approach, based on matching of image spectra to a precomputed library of spectra corresponding to different combinations of depth, bottom type, and water properties, was developed by Louchard et al. (2003) and Mobley (2005) and applied to coral reef mapping in Lesser and Mobley (2007).

Potential users of shallow-water spatial information currently have no objective means to compare and determine the ideal data set(s) and processing approach(es) for their environment, data sets, budget, and processing capabilities. A detailed assessment and comparison of the methods outlined in the preceding paragraph is presented in this work to determine under which conditions these methods work most accurately for mapping and monitoring water depth, water column constituents, and benthic cover types in optically shallow environments. The aim of the work presented in this article was to conduct an independent test of state-of-the-art published shallow water mapping methods using hyperspectral image data and field survey data from Australian sub-tropical and a Commonwealth of the Bahamas tropical locations to identify accuracy and processing time of each mapping algorithm, including variations in image preprocessing after initial atmospheric correction; conditions under which existing mapping models do and don't work; the adaptability of mapping models to two different locations and two imaging sensors; recommended products and procedures for mapping in optically shallow waters; and international best science practice for this type of image-based analysis.

Materials and procedures

Study sites and data sets

The two study sites are Lee Stocking Island, Commonwealth of the Bahamas in the northern hemisphere and Moreton Bay, a subtropical embayment on the eastern Australian Coast near Brisbane in the southern hemisphere (see Fig. 1). These sites were chosen for comparing the hyperspectral inversion methods as they were the best documented and atmospherically corrected airborne imaging spectrometry and in situ data were available without intellectual property restrictions. Both sites were part of several large research projects that provided sufficient field and image data sources, e.g., Lee Stocking (Mobley et al. 2005) and Moreton Bay (Brando et al. 2009; Phinn et al. 2005, 2008; Roelfsema et al. 2006). Table 1 summarizes the bathymetric and benthic survey data and benthic reflectance end members used in this comparison. Airborne imaging spectrometry data were acquired with

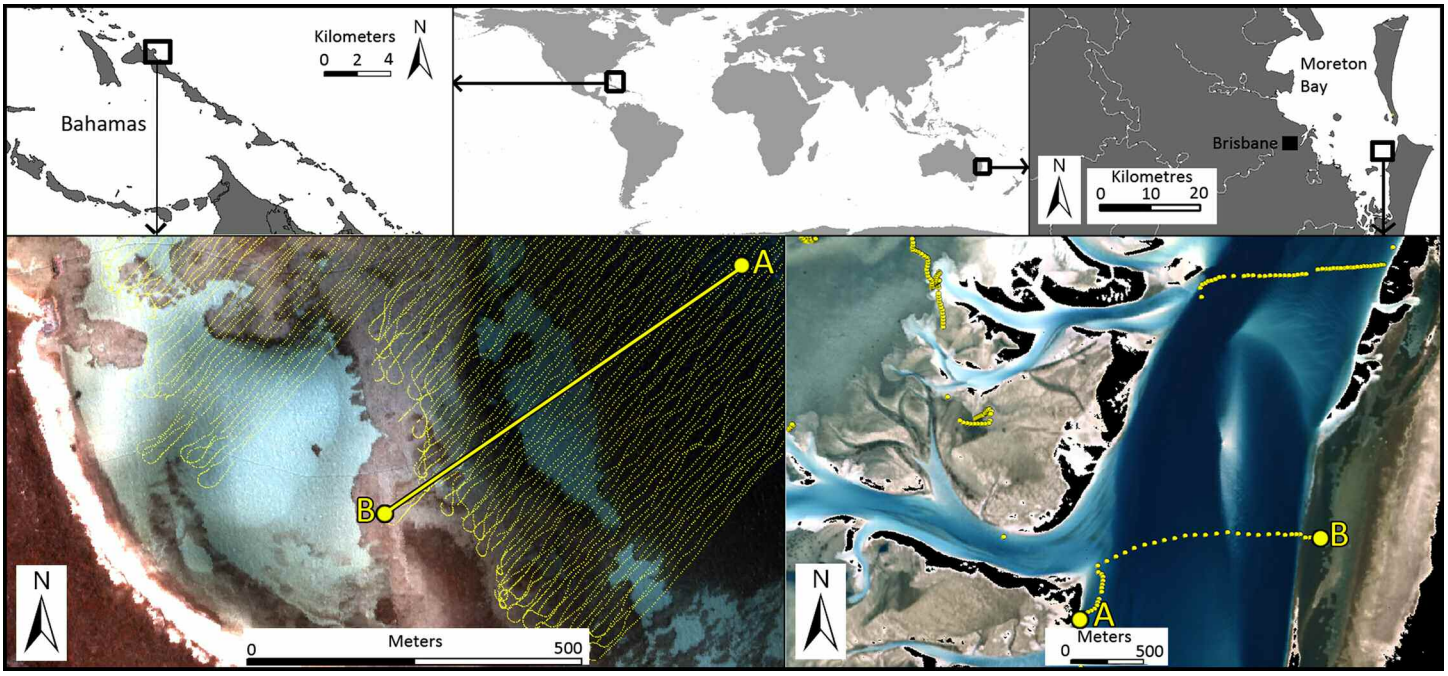

Fig. 1. True color airborne hyperspectral images of the study sites at Lee Stocking Island - Horseshoe Reef and Moreton Bay-Rainbow Channel. Yellow transect lines marked A-B are the location of the acoustic depth transects used to compare image retrieved depth values and measured depth values. In the Lee Stocking Island image, all the acoustic depth transects are shown in thin yellow lines. The Lee Stocking Island image depths vary from 0.0 m in the southwest to 13 m in the northeast. The Moreton Bay image depths vary from 0.0 m on the shallow banks (adjacent to masked out exposed banks) to 10 m deep in the Rainbow Channel.

Ocean PHILLS on 17 May 2000 over LSI using 72 spectral bands of 5 nm wide over 402 to 748 nm and with the CASI-2 airborne imaging spectrometer on 2 July 2004 over the Rainbow Channel in Moreton Bay in imaging mode with 30 bands (10 to 20 nm wide) over the range of 441 to 847 nm. Table 2 describes the image data in more detail including geometric and atmospheric correction. The text below provides additional site information and descriptions of the inherent optical property (IOP) data sets and parameterizations. These study sites were chosen a posteriori to data collection (both in situ and imagery), and therefore, contain different levels and detail of information with respect to parameterization.

Lee Stocking Island, Bahamas

Lee Stocking Island (LSI), Bahamas, is located near 23°46′N, 76°05′W, northwest of Great Exuma Island. The water visibility is often in excess of 10 m, as illustrated by the bottom visibility down to 13 m depth in the LSI image (Fig. 1). The benthos is characterized by carbonate sediments with clean to biofilmed ooid sands, darker sediments, seagrass beds, macroalgae, and patch reefs containing a variety of hard and soft corals (Decho et al. 2003). The water absorption properties are dominated by colored dissolved organic matter (CDOM) derived from decay of benthic biota and displays a strong temporal variation as tides exchange low-CDOM open-ocean water with high-CDOM water from the shallows (Boss and Zaneveld 2003; Mobley et al. 2005). Scattering is influenced by phytoplankton, resuspended sediment, and sub-micrometer mineral particles that can on occasion precipitate out of the high salinity waters in this area (Dierssen et al. 2006).

The available ac-9 measurements (Zaneveld and Boss 2003; Mobley et al. 2005) were used to generate absorption, a, and scattering, b, end member spectra that should bound the likely range of these values at the time of image acquisition (Fig. 2). However, no backscatter data were available. Backscatter measurements in similar waters in the Florida Keys have particle backscatter fractions as high as 0.04 (P. Bissett pers. comm.). Therefore, backscattering spectra b_b were created from the total scattering spectra using assumed particle backscatter fractions B_p of 0.01 and 0.04. The resulting IOP end members were

1. pure water
2. A high-absorption, high-scatter case, with a particle backscatter fraction of $B_p = 0.01$
3. A low absorption, low scatter case; $B_p = 0.01$
4. The same a and b as set 2, but with $B_p = 0.04$
5. The same a and b as set 3, but with $B_p = 0.04$

These five sets of a, b, and b_b end member spectra were defined at 5 nm resolution between 402.5 and 747.5 nm for a total of 70 wavelengths. These wavelengths were later interpolated to the hyper-spectral imager spectral bands.

Rainbow Channel, Moreton Bay, Brisbane, Australia

Moreton Bay (27°30′S, 153°30′E) is a large embayment located on the east coast of Australia. The bay is surrounded by shallow banks to the north and protected by Moreton and

Table 1. Study site water and benthos characteristics and field data sets (See Figs. 2 and 3 for related spectra).

Site	Water Depths & Survey Data	Benthic Composition & Survey Data	Benthic Reflectance Spectra	Water Column composition
Lee Stocking Island, Bahamas	Boat-based depth sounder 12000 points with differential GPS Corrected for tidal height at the time of image acquisition	Not collected	1.clean ooid sand 2.heavily biofilmed sand substrate in a sea grass bed 3."dark sediment" 4.the brightest of the coral spectra 5.the darkest of the coral spectra 6.an average turf algae 7.an average macrophyte 8.an average sea grass (Zhang et al. 2003) (Decho et al. 2003; Dierssen et al. 2003; Louchard et al. 2003), (Stephens et al. 2003)	a440nm 0.02 - 0.12 m^{-1} Chlorophyll a 0.05 - 0.15 mg m^{-3} (Boss and Zaneveld 2003) B_p = 0.01 to 0.04 (no suspended matter concentration used)
Rainbow Channel, Moreton Bay, Australia	Boat-based depth sounder July-August 2004 165 points with standard GPS Corrected for tidal height at the time of image acquisition	56 x 100 m long transects with GPS tagged benthic photographs taken 0.5 m above the bottom at 2 m intervals in July-August 2004. Composition and %-cover of the photographs estimated from 24 sample points. (Phinn et al. 2008)	1. Seagrass species: - *Halophila* ovalis, - *Halophila* spinulosa - *Syringodium* isoetifolium, - *Zostera* muelleri - *Cymodocea* serrulata 2. Brown algae by - *Hydroclatherus* spp. 3. Green algae by *Ulva* spp. 4. Substrate type by: - Brown mud, - Light brown mud - White sand (Roelfsema et al. 2006), (Phinn et al. 2008)	a440 nm 0.025 - 2.63 m^{-1} suspended matter 1.0 and 3.3 g m^{-3} Chlorophyll a 0.4 - 1.0 mg m^{-3} (Brando et al , 2009)

Table 2. Characteristics of the hyperspectral airborne image data sets used for Lee Stocking Island-Horseshoe Reef and Moreton Bay-Rainbow Channel.

Site	Sensor Type	Pixel Size	Spectral Band: - Number - Range - Width	Acquisition Date	Corrections Applied
Lee Stocking Island, Bahamas	Ocean PHILLS	1.3 m	- 128 bands - 400 - 1000 nm - 4.6 nm wide	17 May 2000	Geometric Radiometric:Atmospheric correction using TAFKAA to R_{rs}, trim to 72 bands, 5 nm wide between 402.4 and 747.5 nm (Mobley, Sundman *et al.* 2005)
Rainbow Channel, Moreton Bay, Australia	CASI-2	4.0 m	- 30 bands - 441 – 847 nm - 10 nm wide in 500-680 nm - 20 nm wide in > 680 nm (Brando et al. 2009)	2 July 2004	Geometric Radiometric:Atmospheric correction using c-WOMBAT-c to R_{rs} (Brando et al. 2009)

North Stradbroke Islands on the east and southeast sides (Fig. 1). Moreton Bay is representative of the range of water quality and substratum cover types typically found in eastern Australian coastal and coral reef environments (Phinn et al. 2005, 2008). The Moreton Bay substratum contains significant areas of unconsolidated sediments, ranging from fine-silt muds in the western bay to silicate sands in the eastern bay. Extensive seagrass beds and macro-algae occur throughout the bay, with some bedrock outcrops and fringing reefs, although the latter two do not occur in the imagery used. Due to the number of creeks and rivers that drain into the western part of the bay and the oceanic openings on its eastern side, the water col-

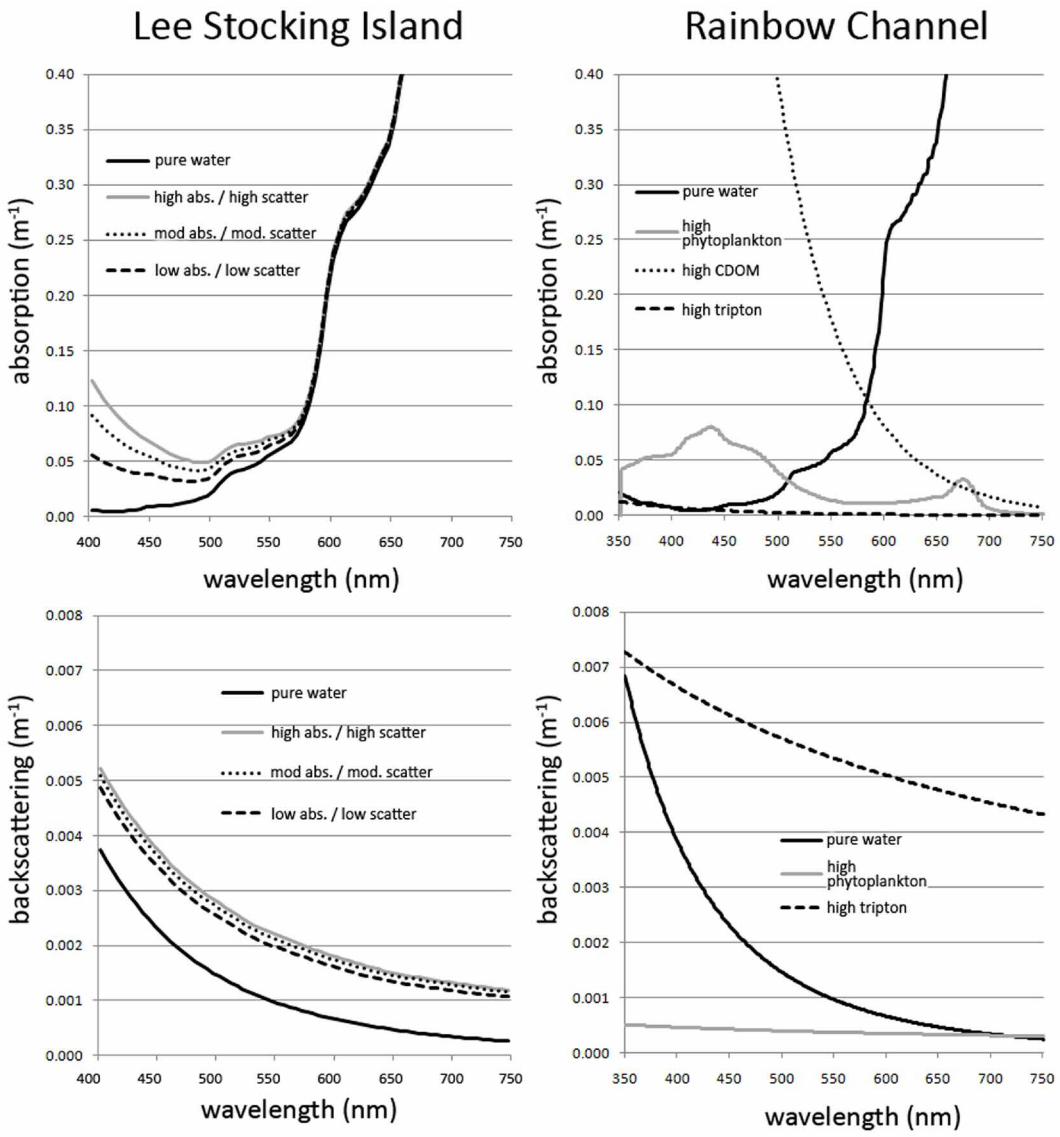

Fig. 2. Inherent optical property end-members for absorption (a) (a440 nm) for Lee Stocking Island-Horseshoe Reef, (b) (a440 nm) for Moreton Bay-Rainbow Channel, (c) back-scattering (b_b555nm) for Lee Stocking Island-Horseshoe Reef, and (d) back-scattering (b_b555nm) for Moreton Bay-Rainbow Channel.

umn usually ranges from freshwater-influenced and often turbid in the western bay to oceanic water–dominated and clear blue-green waters of the eastern Bay (Phinn et al. 2008). Due to the bay's position between several rivers and the ocean, it can have widely varying levels of chlorophyll, suspended matter, and CDOM as function of river run-off, algal blooms, or clear ocean water influx. The study site at Rainbow Channel is near the ocean and will be mainly influenced by ocean water running in and out with some mixing of Moreton Bay water.

The inherent and apparent optical properties (Fig. 3) of Moreton Bay waters were sampled to coincide with an image acquisition and other field surveys from 27 Jul to 3 Aug 2004 during the Australian winter. In-situ absorption, attenuation, backscattering, reflectance, and vertical attenuation were measured at 20 locations in the bay using ac-9, Hydroscat- and TRIOS- Ramses instruments (Phinn et al. 2006; Brando et al. 2009), and water samples were collected for measuring in vivo absorption of CDOM, chlorophyll and NAP, as well as the NAP and chlorophyll concentrations. All measurements were carried out following (Brando et al. 2009; Oubelkheir et al. 2006; Phinn et al. 2006).

Based on these field data the fixed values for seven SIOP scalar parameters (S_{CDOM}, S_{NAP}, a^*_{NAP} (440 nm), b^*_{bphy} (542 nm), b^*_{bNAP} (542 nm), Y_{phy}, and Y_{NAP}) as well the Chlorophyll *a* specific absorption spectrum $a^*_{phy}(\lambda)$ were estimated (Brando et al. 2009). The values of the SIOP parameters for this study are

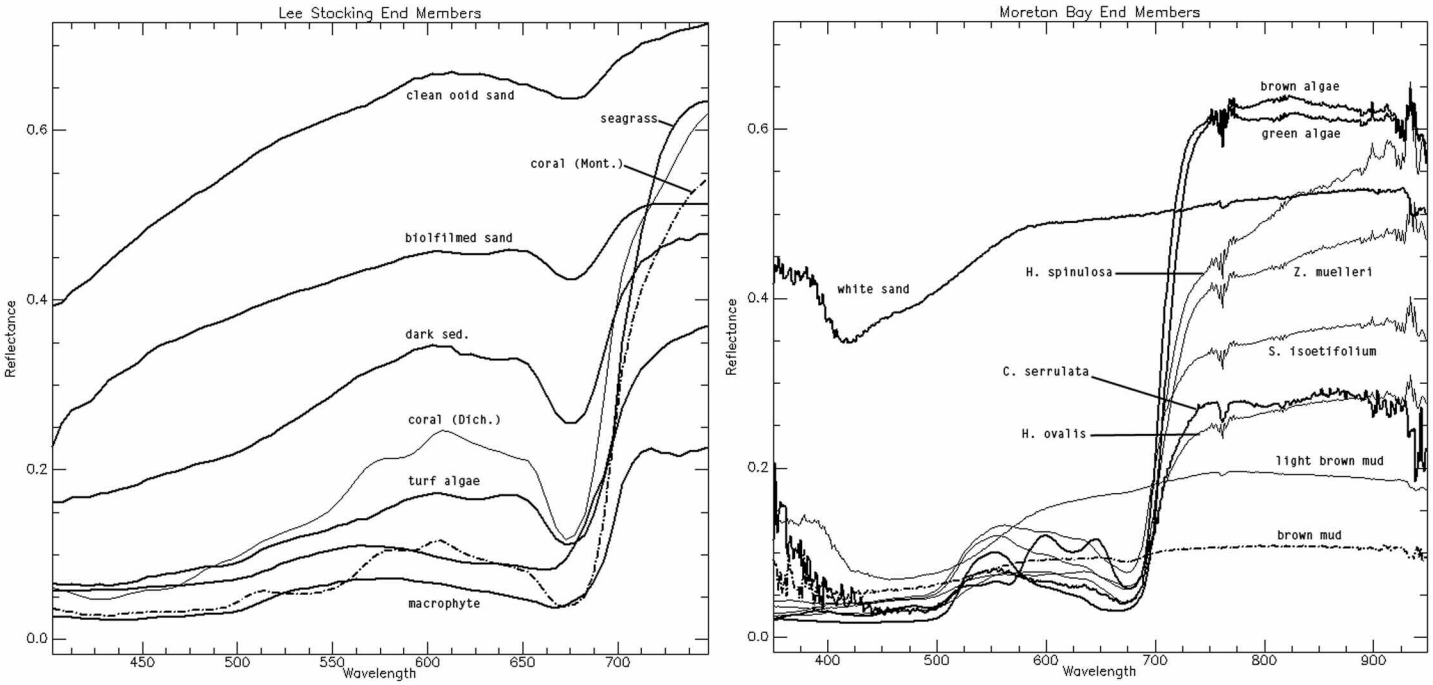

Fig. 3. Benthic reflectance spectra used as end-members in each inversion method for Lee Stocking Island-Horseshoe Reef and Moreton Bay-Rainbow Channel data sets. Reflectance spectra measurement approaches are outlined in (Phinn et al. 2008) and (Mobley et al. 2005).

similar to those reported previously for Moreton Bay and other Australian coastal waters (Brando and Dekker 2003; Oubelkheir et al. 2006; Qin et al. 2007; Blondeau-Patissier et al. 2009).

Optically shallow water inversion procedures

Many approaches have been developed for inversion of remote-sensing reflectances to obtain shallow-water bathymetry and other environmental information. One of the oldest published algorithms for bathymetry is the empirical multispectral technique of Polcyn et al. (1970), later modified by Lyzenga (1981). This algorithm can accurately retrieve bathymetry, but only in areas of constant water clarity and homogenous benthos/substrate composition, and it cannot retrieve water-column IOPs. Because of its historical importance and continued widespread and somewhat successful use under certain conditions, we present bathymetry obtained by application of the Lyzenga algorithm to our hyper-spectral imagery for comparison with the more general techniques discussed here.

Statistical or empirical band-ratio bathymetry algorithms, such as Lyzenga's, can be tuned to specific data sets, e.g., Dierssen et al. 2003. However, band-ratio algorithms are generally limited by the non-uniqueness of the ratios as functions of depth, water IOPs, and bottom reflectance. More sophisticated nonlinear inversion techniques, such as neural networks, can provide good retrievals provided that an adequate database from field data or forward bio-optical modeling is used to connect remote sensing reflectances with environmental conditions. An in-situ measurement-based neural network training requirement ties the neural network to the environment represented in the training data. A neural network trained by forward modeling (employing radiative transfer or analytical models) is limited only by the range of inputs used in the forward model to generate the pseudo-data.

In this intercomparison, we consider only those inversion algorithms that make full use of radiometrically calibrated hyperspectral remote-sensing reflectances, R_{rs}. These inversion algorithms can all, in principle, function without in-situ information regarding deep-water pixels or ancillary observations made at the location of interest. These inversion algorithms do, in general, become more accurate with increased a priori parameterization.

For this exercise, we consider several variants of the semi-analytical method first developed by (Lee et al. 1999; Lee et al. 1998b). In this inversion method, the radiative transfer equation (RTE) is simplified so that only a few parameters remain (e.g., water depth, bottom reflectance, and water absorption and backscatter at one wavelength), whose values can then be determined by an optimization technique applied to measured R_{rs} spectra. We also consider an inversion method (Mobley et al. 2005) in which the RTE is not simplified, but which uses numerical solutions of the RTE to build up a database of reflectance spectra that correspond to a wide range of environmental conditions. These database spectra are then matched to the image spectra to obtain a retrieval of the environmental conditions. This inversion method is not tied to site-specific data sets and thus has the potential to be applied

to a broader range of environments, provided the database is sufficiently representative of those additional environments. These techniques all provide a simultaneous retrieval of bathymetry, bottom classification, and water column IOPs.

The five methods compared were referred to as HOPE, BRUCE, SAMBUCA, CRISTAL, and ALLUT. All these methods rely on some form of spectrum matching of modeled reflectance spectrum using a set of bathymetry, bottom classification, and water column IOPs values, optimized to match the image R_{rs} spectra. HOPE, BRUCE, and SAMBUCA perform spectrum matching via a nonlinear search that determines the optimal parameter values for their semi-analytical model, while CRISTAL performs spectrum matching by searching through a precomputed database of R_{rs} spectra. ALLUT is a hybrid application that merges these two approaches. ALLUT uses an adaptive LUT method for creating an effective look up table (LUT) for parameterizing the semi-analytical model and then applies spectrum matching. Each approach simplifies the RTE or the inversion of the RTE and its parameters in a slightly different manner (Table 3). The resulting tradeoffs are that HOPE, BRUCE, and SAMBUCA assume a limited set of absorption backscattering and bottom reflectance spectra, ALLUT uses an adaptive LUT method for parameterizing the IOPs, whereas the CRISTAL has to model all relevant combinations of bathymetry, bottom classification, and water column IOPs, representative of the imaged environment. The accuracy of the retrieved parameters from HOPE, BRUCE, SAMBUCA depends on the adequacy of their underlying semi-analytic model and input parameters to represent the environment, and CRISTAL and ALLUT results rely on whether or not the LUT database contains IOP and benthic/substrate spectra representative of those in the imaged area.

In terms of application purposes, the BRUCE method was developed for processing large amounts of HyMap data for whole of reef systems (100s km) rocky reef and sea grass areas in waters from zero depth to optically deep. The SAMBUCA method was developed to deal with all optically shallow through to optically deep aquatic ecosystems. The HOPE and CRISTAL methods were developed for defense purposes mainly and specialize in estimating bathymetry in inaccessible or denied areas where a priori information may not be available. ALLUT is a recent development that incorporates parts of the HOPE, SAMBUCA, and the CRISTAL approaches, and is thus a hybrid version building forth on these developments. Each of the techniques and their application to the test data sets is outlined below and uses the parameter settings outlined in Tables 3 and 4. As the inversion methods were developed for different applications the pre-processing of input imagery varied per method. A decision was made to compare the methods as they are published in literature—including preprocessing variations that may influence the performance outcomes. Thus this study compares complete methods rather than focusing solely on the performance of the RTE-based inversion (where one would need to presume exact same spectral reflectance inputs).

Hyperspectral optimization process exemplar model (HOPE)

Remote-sensing reflectance (R_{rs}) is the fundamental property for inversion of subsurface properties, such as the water column or bottom composition. For optically shallow waters, R_{rs} not only depends on the absorption and scattering properties of dissolved and suspended materials in the water column but also on the depth and reflectivity of the bottom. R_{rs} is also influenced by contributions from inelastic scattering such as

Table 3. Summary of the parameters and parameter values used for each inversion model.

	HOPE LSI	HOPE MB	BRUCE LSI	BRUCE MB	SAMBUCA LSI	SAMBUCA MB	CRISTAL LSI	CRISTAL MB	ALLUT LSI	ALLUT MB
Initial parameterisation	(value or range)									
P	0.05(Rrs(440)/Rrs(550)^-1.7	/Rrs(550)^-1.7	0.05(Rrs(440)/Rrs(550)^-1.7	0.05(Rrs(440)/Rrs(550)^-1.7					0.00 - 1.58	
G	1.5 P	1.5 P	1.5 P	1.5 P					0.00 - 1.048	
Scdom	0.015	0.015			0.0183	0.0157				
X	8 Rrs(660)	8 Rrs(660)	8 Rrs(660)	8 Rrs(660)					0.00 - 0.075	
B	4 Rrs(490)	4 Rrs(490)					0.01, 0.02 ..0.04	0.01 or 0.03		0.0183
H	1/6P	1/6P								
Y	0.50	0.50	1.00	1.00					0.42	
C_chl					0.15 (0.01 - 0.02)	0.7 (0.1 - 20.0)				0.10 - 20.00
b*bphy(542)					0.00038	0.00038				
Yphy					1.178	0.681				
C_cdom					0.08 (0.008 - 0.15	0.07 (0.01 - 1.00)				0.01 - 1.00
C_nap					0.15 (0.01 - 0.30)	2.8 (1.0 - 3.3)				0.10 - 10.00
a*nap(440)					0.005	0.0048				
S_nap					0.0101	0.0106				
r_rs to R-rs			0.54, 1.5						0.5, 1.5	0.55, 1.5
Depth(m)					Limited by NedR to SDI calculation	Limited by NedR to SDI calculation	0.01-optically deep in discrete intervals (N=84)	0.01-optically deep in discrete intervals (N=42)	0.00 - 20.00	0.00 - 20.00
Benthic model	Sand + grass	Sand + grass	every combination of 8 spectra over 3	every combination of 10 spectra over 3 classes	every combination of 2 spectra out of 8	every combination of 2 spectra out of 10	discrete combinations of 2 to 4 spectra out of 8	discrete combinations of 2 to 4 spectra out of		
Nr of endmembers (or combinations)	2	2	24	30	28	45	39	71		

Table 4. Composition of benthic cover classes (in terms of bottom irradiance reflectance endmembers) used for mapping benthic cover classes from retrieved R_b values in (a) Lee Stocking Island-Horseshoe Reef and (b) Moreton Bay-Rainbow Channel.

(a) **Sediment**	**Vegetation**	**Coral**
(1) clean ooid sand	(1) avg. turf algae	(1) coral (*Montastria*)
(2) Biofilmed sand in seagrass bed	(2) avg. macrophyte	(2) coral (*Dichocoenia*)
(3) dark sediment	(3) avg. sea grass	(3) avg. turf algae

(b) **Sediment**	**Green vegetation**	**Green/Brown Vegetation**
(1) white Sand	*(1) Zostera muelleri*	(1) brown algae
(2) brown Mud	*(2) Halophila ovalis*	*(2) Zostera muelleri*
(3) light brown Mud	*(3) Halophila spinulosa*	*(3) Halophila ovalis*
	(4) Syringodium isoetifolium	*(4) Halophila spinulosa*
	(5) Cymodocea serrulata	*(5) Syringodium isoetifolium*
	(6) green algae	*(6) Cymodocea serrulata*
		(7) green algae

fluorescence and Raman emission (Marshall and Smith 1990; Lee et al. 1994). However, in optically shallow waters, water column inelastic scattering contributes relatively little to the water leaving radiance and is ignored. The spectral R_{rs} can be conceptually summarized as

$$R_{rs}(\lambda) = f[a(\lambda), b_b(\lambda), \rho(\lambda), H, \theta_w, \theta_v, \varphi] \quad (1)$$

where $a(\lambda)$ is the absorption coefficient, $b_b(\lambda)$ is the backscattering coefficient, $\rho(\lambda)$ is the benthic spectral reflectance, H is the bottom depth, θ_w is the sub-surface solar zenith angle, θ_v is the subsurface viewing angle from nadir, and φ is the viewing azimuth angle from the solar plane.

Historically, for the derivation of bathymetry, values for water-column contributions were approximated from values of adjacent deep waters (Polcyn et al. 1970; Lyzenga 1981; O'Neill et al. 1988), or empirically derived from an image by regression using a few true depths provided by LIDAR or on-site ship measurements (Lyzenga 1981; Philpot 1989). For denied places or regions of no a priori knowledge of water properties, clearly properties of both the water column and the bottom will have to be derived at the same time. To reach this goal, Lee et al. (1999) developed a model-driven spectral optimization technique (Hyper-spectral Optimization Process Exemplar, HOPE), which is summarized here.

Based on Hydrolight simulations, R_{rs} of optically-shallow water with $\varphi = 90°$ is analytically approximated as Lee et al. (1999)

$$\begin{aligned} R_{rs} &\approx \frac{\Gamma}{1-\varsigma r_{rs}} r_{rs}, \\ r_{rs} &\approx r_{rs}^{dp}\left[1-\exp\left(-\left(\frac{1}{\cos(\theta_w)}+\frac{D_u^C}{\cos(\theta_v)}\right)\kappa H\right)\right]+ \\ &\quad \frac{1}{\pi}\rho\exp\left(-\left(\frac{1}{\cos(\theta_w)}+\frac{D_u^B}{\cos(\theta_v)}\right)\kappa H\right), \end{aligned} \quad (2)$$

with

$$\kappa = a + b_b,\ u = b_b/(a + b_b) \quad (3)$$

$$D^C_u \approx 1.03(1 + 2.4u)^{0.5}, \text{ and } D^B_u \approx 1.04(1 + 5.4u)^{0.5} \quad (4)$$

and,

$$b_b = b_{bw} + b_{bp}, \quad (5)$$

$$a = a_w + a_{phy} + a_g. \quad (6)$$

Here r_{rs} is the sub-surface remote-sensing reflectance, or ratio of the upwelling radiance to downwelling irradiance evaluated just below the surface, b_{bw} is the backscattering coefficient of pure seawater, while b_{bp} is the backscattering coefficient of suspended particles. a_{phy} is the absorption coefficient for phytoplankton pigments, and a_g is the absorption coefficient for gelbstoff and detritus (Carder et al. 1999). Two optical path-elongation factors: one for photons from the water column (D^C_u), and the other for photons from bottom (D^B_u). These are approximated as in Lee et al (1999). Wavelength dependence, unless necessary, is omitted for brevity.

Note that both u and κ are inherent optical properties, and it is the combination of Eqs.2-6 that provides the expression for R_{rs}. In Eq.2, Γ is the water-to-air divergence factor (Mobley 1994), and $(1-\varsigma\, r_{rs})$ accounts for the internal reflection of the water-air interface, which is important when r_{rs} values are high for very shallow and/or very turbid waters.

The first term on the right side of the r_{rs} equation (Eq.2) expresses the portion of the path radiance expected for the presence of a black bottom with depth H, whereas the second term expresses the bottom contribution propagated to the surface after attenuation by the two-way path through the water column. r_{rs}^{dp} is the remote-sensing

reflectance for optically deep waters for which various models have been developed.

When $R_{rs}(\lambda)$ is provided from any spectrometer, retrieval of subsurface properties becomes a mathematical problem: deriving the quantities of interest by spectrally decomposing Eq. 2. If there are *n* independent channels that have valid R_{rs}, Eq. 2 is:

$$\begin{aligned} R_{rs}(\lambda_1) &= F(a_w(\lambda_1), b_{bw}(\lambda_1), a_\phi(\lambda_1), a_g(\lambda_1), b_{bp}(\lambda_1), \boldsymbol{\rho}(\lambda_1), H) \\ R_{rs}(\lambda_2) &= F(a_w(\lambda_2), b_{bw}(\lambda_2), a_\phi(\lambda_2), a_g(\lambda_2), b_{bp}(\lambda_2), \rho(\lambda_2), H) \\ &\vdots \\ R_{rs}(\lambda_n) &= F(a_w(\lambda_n), b_{bw}(\lambda_n), a_\phi(\lambda_n), a_g(\lambda_n), b_{bp}(\lambda_n), \rho(\lambda_n), H) \end{aligned} \quad (7)$$

In this series of equations, there are at least 4 unknown spectra [$a_{phy}(\lambda)$, $a_g(\lambda)$, $b_{bp}(\lambda)$, and $\rho(\lambda)$] and 1 scalar unknown (H) for each R_{rs} spectrum, as values of $a_w(\lambda)$ and $b_{bw}(\lambda)$ are known (Pope and Fry 1997; Morel 1974). This suggests that for n equations, there are (4n + 1) unknowns to be deduced. To mathematically solve for this many unknowns, additional relationships have to be established to reduce the number of unknowns (or increase the number of equations).

$a_{phy}(\lambda)$ is simulated by a single-parameter model (Lee et al. 1998a):

$$a_{phy}(\lambda) = [a_0(\lambda) + a_1(\lambda) \ln(P)]\, P, \quad (8)$$

with $P = a_{phy}(440)$, the variable for phytoplankton absorption coefficient at 440 nm. This approach allows $a_\phi(\lambda)$ curvature to change with $a_{phy}(440)$ value, consistent with field observations, at least to first order.

$a_g(\lambda)$ is expressed as (Bricaud et al. 1981; Carder et al. 1999)

$$a_g(\lambda) = G\, e^{-S(\lambda - 440)}, \quad (9)$$

with $G = a_g(440)$. S is the spectral slope, and a global average value of 0.015 nm^{-1} is used as a default.

$b_{bp}(\lambda)$ is expressed as

$$b_{bp}(\lambda) = X\left(\frac{550}{\lambda}\right)^Y, \quad (10)$$

where $X = b_{bp}(550)$, and *Y* is the spectral shape parameter of particle backscattering, which could be estimated via empirical relationships. As in Lee et al. (2001), a default value of 0.5 is used for all the pixels of this study.

$\rho(\lambda)$ is expressed as

$$\rho = B\rho^+ \quad (11)$$

with *B* the bottom albedo value at 550 nm, and ρ the 550 nm-normalized spectral shapes of a specific bottom type. Although multiple bottom types could be incorporated into the semi-analytical model, the current default version of HOPE incorporates sand-albedo (ρ^+_{sand}) and grass-albedo (ρ^+_{grass}), and the following empirical criteria is used to select the bottom spectral shape: if $R_{rs}(\lambda)$ of a pixel satisfies

$$R_{rs}(550) < 0.01 \text{ and } R_{rs}(710)/R_{rs}(670) > 1.2, \quad (12)$$

ρ^+_{grass} is used; otherwise, ρ^+_{sand} is used, and each pixel is assumed homogeneous in bottom type.

After the above empirical/semi-analytical models are assembled, Eq.7 becomes explicit functions of *P, G, X, B,* and *H*:

$$\begin{aligned} R_{rs}(\lambda_1) &= F(a_w(\lambda_1), b_{bw}(\lambda_1), \boldsymbol{P, G, X, B, H}) \\ R_{rs}(\lambda_2) &= F(a_w(\lambda_2), b_{bw}(\lambda_2), \boldsymbol{P, G, X, B, H}) \\ &\vdots \\ R_{rs}(\lambda_n) &= F(a_w(\lambda_n), b_{bw}(\lambda_{\boldsymbol{n}}), \boldsymbol{P, G, X, B, H}) \end{aligned}. \quad (13)$$

HOPE numerically solves for the 5 unknowns in Eq.13 via spectral optimization, i.e., to minimize an objective function (Eq.14) that compares modeled and measured spectral R_{rs}. When this function is minimized (optimal consistency between measured and modeled R_{rs}), the values of *P, G, X, B,* and *H* that makes up the modeled R_{rs} are considered as the solutions. The objective function is defined as

$$err = \frac{\left[\sum_{400}^{675}\left(R_{rs} - \hat{R}_{rs}\right)^2 + \sum_{750}^{800}\left(R_{rs} - \hat{R}_{rs}\right)^2\right]^{0.5}}{\sum_{400}^{675} R_{rs} + \sum_{750}^{800} R_{rs}}, \quad (14)$$

with $\hat{R}_{rs}$ for values from Eq. 13 and R_{rs} for values from measurements. The cutoff between 675 and 750 nm is trying to avoid the influence of solar-stimulated chlorophyll fluorescence, which is present in measured R_{rs} but not in the model. For significantly shallow bottoms (<1 m), this spectral window needs to be included in the inversion, however.

In the HOPE process, values of *P, G, X, B,* and *H* are initiated pixel-wise (see Lee et al. 1999) as

$$\begin{aligned} P &= 0.05\left(\frac{R_{rs}(440)}{R_{rs}(550)}\right)^{-1.7} \\ G &= 1.5\, P \\ X &= 8\, R_{rs}(660) \\ B &= 4\, R_{rs}(490) \\ H &= \frac{1}{6\, P} \end{aligned} \quad (15)$$

In the whole inversion process, there is no field data are required/used except the measured $R_{rs}(\lambda)$ spectrum. Traditional empirical algorithms for bathymetry, however, require many assumptions and ground truth data before the derivation of bottom depth.

Preprocessing of image data before HOPE application

To minimize the impacts on retrievals from erroneous images, spectral R_{rs} was preprocessed before feeding to HOPE.

This preprocess contains two aspects: 1) spatial smoothing for wavelengths longer than 600 nm; and 2) white correction for each pixel. Process 1 reduces image speckle resulting from low signals in the longer wavelengths of the hyper-spectral images. Process 2, on the other hand, compensates, to a degree, for over- or under-correction of the atmospheric effects (including surface reflectance). This process is the same as those described in Lee et al. (2001), i.e., it has the following steps.

Assume R_{rs}^{raw} as the product from an image,

$$\begin{aligned} R_{rs}^{1}(\lambda) &= R_{rs}^{raw}(\lambda) - R_{rs}^{raw}(750) \\ \Delta &= 0.0001 + 0.02 R_{rs}^{1}(650) \\ R_{rs} &= R_{rs}^{1}(\lambda) + \Delta \end{aligned} \tag{16}$$

This final R_{rs} is then fed to HOPE to derive sub-surface properties via spectral optimization.

Bottom reflectance un-mixing computation of the environment model (BRUCE)

The BRUCE inversion model incorporates the semi-analytic HOPE model developed by Lee et al. (1999) (see Eqs. 1-16), with a modification to the bottom reflectance parameterization (Klonowski et al. 2007). In the BRUCE model, the bottom reflectance term, ρ, is parameterized by the linear combination of three bottom reflectance spectra that are representative of three key benthic cover classes, namely sediment, vegetation, and coral. For situations where more than three spectral end members are available, such as this study, the end members are typically separated into their three respective key benthic classes, which allows for various combinations of 3 bottom types by selecting in turn one member from each of the three benthic classes. The bottom reflectance parameterization is thus expressed as,

$$\rho(\lambda) = B_{sed_i}\rho_{sed_i}(\lambda) + B_{veg_i}\rho_{veg_i} + B_{cor_i}\rho_{cor_i}(\lambda); B_{sed_i} + B_{veg_i} + B_{cor_i} = 1 \tag{17}$$

where B_{sed_i}, B_{veg_i}, and B_{cor_i} correspond to the fractional weighting coefficient of bottom reflectance spectra within the benthic classes: sediment, vegetation, and coral, respectively. $\rho_{sed_i}(\lambda)$, $\rho_{veg_i}(\lambda)$, and $\rho_{cor_i}(\lambda)$ are the measured bottom reflectance spectral end members in each key benthic cover class.

The water column absorption and backscattering coefficients are parameterized with P, G, X, and Y as in the HOPE method. We keep the spectral slope of backscattering, Y, fixed to a value of 1.0. The BRUCE model is therefore described by 7 model parameters (P, G, X, B_{sed_i}, B_{veg_i}, B_{cor_i} and H). Inversion is performed with Levenberg-Marquardt optimization. For each image pixel, optimization is achieved by iterating through all combinations of 3-bottom types and varying the parameters P, G, X, B_{sed_i}, B_{veg_i}, B_{cor_i}, and H. The combination of retrieved parameters with the best model fit to the measured R_{rs} spectrum is determined and the associated retrieved model parameters, including the benthic class end member indexes, are saved.

Preprocessing of LSI image data before BRUCE application

The 8 LSI bottom reflectance spectra (substrate end members) were grouped into three key substrate classes: sediment, vegetation, and coral (Table 4a). The brown algae (avg. turf algae) end member was also included in the coral class to account for situations where green and brown vegetation may occur together. This results in 24 unique end member combinations of three substrates.

Each image R_{rs} spectrum was corrected by subtracting 0.003 Sr^{-1} to account for the observed atmospheric under correction unit of steradian should be sr not Sr (Klonowski et al. 2007). A further correction was performed to account for sunglint contamination using the assumption that R_{rs} at near infrared (NIR) wavelengths are approximately zero. One must note however that this assumption does not necessarily hold true for all shallow waters where NIR signals from the seafloor can be a contributing factor in very shallow clear waters. We mask out the shallow water pixels by performing a linear regression of R_{rs} versus wavelength over the spectral range 610 nm to 900 nm. For pixels where the calculated slope was less than or equal to –2, it was assumed the spectra were likely to be representative of shallow waters and were masked out from the sunglint correction. For nonmasked pixels the following sunglint correction was performed:

$$R_{rs}^{SGC}(\lambda) = R_{rs}(\lambda) - median\left[R_{rs}(650nm:800nm)\right] \tag{18}$$

where, $R_{rs}^{SGC}(\lambda)$ is the sunglint-corrected R_{rs}.

Processing of LSI image data with BRUCE

Image inversion was performed over the first 72 PHILLS channels (402.5 to 747.5 nm range) with all wavelengths weighted evenly.

Preprocessing of MB image data before BRUCE application

The 10 MB bottom reflectance spectra (substrate end members) were grouped into three key substrate classes: sediment, green vegetation, and green/brown vegetation (Table 4b). The 6 green vegetation end members were included in the green/brown vegetation class in an attempt to account for different mixtures of seagrasses. A total of 63 unique end member combinations were available for MB image inversion.

The standard BRUCE data processing software requires R_{rs} as the input. Thus, the MB image irradiance reflectance spectra just below the sea surface, R(0-), were converted to above-water remote sensing reflectance, R_{rs}, using:

$$R_{rs} = 0.54\ R(0-)/Q = 0.135\ R(0-), \tag{19}$$

where Q = 4. No other manipulation of the image spectra was performed before the inversion process.

Processing of MB image data with BRUCE

Image inversion was performed over the first 25 CASI chan-

nels (439.3 and 732.5 nm range) with all wavelengths weighted evenly.

Semi-analytical model for bathymetry, un-mixing, and concentration assessment (SAMBUCA)

SAMBUCA, is an implementation of the inversion/optimization method by (Lee et al. 1999; 2001) (Eqs. 1-15) enhanced to: 1) retrieve the concentrations of optically active constituents in the water column (Chl *a*, CDOM, and NAP), 2) account for more than one substratum cover type, and 3) to estimate the contribution of the substratum to the remote sensing signal (Brando et al. 2009).

The absorption and backscattering coefficients are described as the sum of the contributions of N constituents and a constant coefficient for pure water:

$$a = a_w + \sum_{j=1}^{N} a_j^* C_j; b_b + b_{bw} + \sum_{j=1}^{N} b_{bj}^* C_j \quad (20)$$

where a_w and b_{bw} are the absorption and backscattering of pure water (Morel 1974; Pope and Fry 1997), a_i^* and b_{bi}^* are the specific inherent optical properties (SIOPs) of jth constituent with concentration C_j. In the formulation of equation CDOM has no backscattering term associated with it, and a_{CDOM} (440 nm) represents the concentration of CDOM.

The nonwater absorption terms are parameterized as a known shape with an unknown magnitude:

$$a_{phy}(\lambda) = C_{CHL} \cdot a_{phy}^*(\lambda) \quad (21)$$

$$a_{CDOM}(\lambda) = C_{CDOM} \cdot a_{CDOM}^*(\lambda_0) \exp\left[-S_{CDOM}(\lambda - \lambda_0)\right] \quad (22)$$

$$a_{NAP}(\lambda) = C_{NAP} \cdot a_{NAP}^*(\lambda_0) \exp\left[-S_{NAP}(\lambda - \lambda_0)\right] \quad (23)$$

where C_{CHL} is the concentration of Chl *a* and $a_{phy}^*(\lambda)$ is the Chl *a* specific absorption spectrum. As the concentration of CDOM (C_{CDOM}) is represented by a_{CDOM} (440 nm), the reference wavelength λ_0 was set at 440 nm, S_{CDOM} is the spectral decay constant for CDOM absorption coefficient, and $a_{CDOM}^*(\lambda_0)$ is set to 1. C_{NAP} is the concentration of NAP; $a_{NAP}^*(\lambda_0)$ is the specific absorption of NAP at the reference wavelength, and S_{NAP} is the spectral slope constant for NAP absorption coefficient; and the reference wavelength λ_0 was set at 440 nm for NAP absorption coefficient.

The nonwater backscattering terms are parameterized as follows:

$$b_{bp} = b_{bphy} + b_{bNAP} \quad (24)$$

$$b_{bphy}(\lambda) = C_{CHL} \cdot b_{bphy}^*(\lambda_0) \left(\frac{\lambda_0}{\lambda}\right)^{Y_{phy}} \quad (25)$$

$$b_{bNAP}(\lambda) = C_{NAP} \cdot b_{bNAP}^*(\lambda_0) \left(\frac{\lambda_0}{\lambda}\right)^{Y_{NAP}} \quad (26)$$

where $b_{bphy}^*(\lambda_0)$ is the specific backscattering of algal particles at the reference wavelength, Y_{phy} the power law exponent for the algal particles coefficient; $b_{bNAP}^*(\lambda_0)$ is the specific backscattering of NAP at the reference wavelength, Y_{NAP} the power law exponent for NAP backscattering coefficient. The reference wavelength λ_0 was set at 542 nm for both algal and nonalgal particle backscattering coefficient.

In SAMBUCA, the algorithm by Lee et al. (1999; 2001) was modified to account for more than one substratum cover type in a pixel or spectrum by expressing the bottom albedo A(λ) as linear combination of two substrata:

$$\rho(\lambda) = B_i \rho_i(\lambda) + B_j \rho_j(\lambda); B_i + B_j = 1 \quad (27)$$

where B_i and B_j represents the fractional cover of substratum i and substratum j within each pixel, ρ_i (λ) and ρ_j (λ) are the spectral benthic reflectance of substratum i and j, respectively. When solving for more than two cover types, SAMBUCA cycles through a given spectral library, retaining those two substrata and their estimated fractional cover q_{ij}, which achieve the best spectral fit.

In summary, the complete model parameterization for SAMBUCA is:

$$r_{rs}^{\mathrm{model}} = f\begin{pmatrix} C_{CHL}, C_{CDOM}, C_{NAP}, H, B_i, \rho_i(\lambda), \rho_j(\lambda), S_{CDOM}, S_{NAP} \\ Y_{PHY}, Y_{NAP}, a_{PHY}^*(\lambda), a_{NAP}^*(\lambda_0), b_{bPHY}^*(\lambda_0), b_{NAP}^*(\lambda_0) \end{pmatrix} \quad (28)$$

In SAMBUCA, the algorithm by (Lee et al. 1999; (Brando et al. 2009) was modified to estimate the contribution of the substratum to the subsurface remote-sensing reflectance signal by comparing the modeled spectrum using an optically deep system ($r_{rs}^{\mathrm{dp\_model}}$, i.e., the term indicated as r_{rs}^{dp} in Eq. 2), and the modeled spectrum for an optical shallow water body as generated by SAMBUCA (r_{rs}^{model}).

To provide a quantitative indication of the contribution of the substratum to the subsurface remote-sensing reflectance signal of the water body (Brando et al. 2009) introduced the Substratum Detectability Index defined as the absolute value of the spectral substratum detectability for the band of maximum penetration:

$$SDI = \max\left(\left|r_{rs}^{\mathrm{model}} - r_{rs}^{dp\_\mathrm{model}}\right| / \mathrm{NE}\Delta r_{rsE}\right) \quad (29)$$

This quantity is sensor dependent and scene dependent: it quantifies the contribution of the substratum to the subsurface remote-sensing reflectance signal for a given sensor as it uses the noise equivalent difference in reflectance ($\mathrm{NE}\Delta r_{rsE}$) as a scaling factor. SDI allows three classes of waters to be identified in the imagery: "optically shallow waters" where the signal from the substratum is directly measurable and the substratum signal at the surface is more than 5 $\mathrm{NE}\Delta r_{rsE}$ at the band of maximum penetration (SDI > ~5); "quasi-optically deep waters," where the contribution from

the substratum is weak and the substratum signal at the surface is between 1 and 5 $NE\Delta r_{rsE}$ (i.e., 1 < SDI < 5); and "optically deep waters," where no signal from the substratum is measurable (i.e., SDI = 0).

For optically deep waters (i.e., SDI = 0), the estimate of depth is not possible as no signal from the substratum is measurable. Because of that, the retrieved values of the water depth from the inversion/optimization can be any of the values deeper than the depth than sets SDI to 0, leading to an overestimate of the real depth for those pixels. To retrieve an "as shallow as possible" depth when an optically deep solution is encountered at the end of a SAMBUCA inversion optimization, a secondary iteration was introduced. The retrieved depth for the optically deep pixels is iteratively decreased while maintaining SDI = 0. This secondary iteration ensures the retrieval of an "as shallow as possible" depth value for each pixel.

In the inversion-optimization scheme in SAMBUCA, r_{rs}^{model} is compared to r_{rs}^{input} using a goodness-of-fit or error function. The set of variables that minimizes the difference between these two spectra is used to estimate the environmental variables being sought, e.g., water column depth, substratum composition, and the concentrations of the optically active constituents of the water column.

For the inversion-optimization in SAMBUCA, the Downhill Simplex method was adopted. In SAMBUCA, the optimization residuum, Δ, is quantified with a hybrid formulation that combines the spectral matching function (e.g., Spectral Angle Mapper in Kruse et al. 1993) and the least squares minimum to balance the requirements for spectral shape and magnitude matching:

$$\Delta = \alpha \times LSQ \tag{30}$$

where, α[rad] is the spectral angle between reference spectra and the spectra of the pixel in question as defined in the SAM (Kruse et al. 1993) by

$$\alpha = \cos^{-1} \frac{\sum_{i=1}^{N} w(\lambda_i) * \left(r_{rs}^{\text{model}}(\lambda_i) * r_{rs}^{\text{input}}(\lambda_i) \right)}{\left[\sum_{i=1}^{N} \left(w(\lambda_i) * r_{rs}^{\text{model}} \right)^2 \right]^{1/2} \left[\sum_{i=1}^{N} \left(w(\lambda_i) * r_{rs}^{\text{input}}(\lambda_i) \right)^2 \right]^{1/2}} \tag{31}$$

and LSQ is the least square distance:

$$LSQ \frac{\left[\sum_{i=1}^{N} w(\lambda_i) * \left[r_{rs}^{\text{model}}(\lambda_i) - r_{rs}^{\text{input}}(\lambda_i) \right]^2 \right]^{1/2}}{\sum_{i=1}^{N} w(\lambda_i) * r_{rs}^{\text{input}}(\lambda_i)} \tag{32}$$

The weighting function, $w(\lambda_i)$, can be introduced for both LSQ and α to weight the contribution of different wavelength bands. For both datasets $w(\lambda_i)$ was set to $1/NE\Delta r_{rsE}$ to discount the wavelengths where the signal is less accurate or noisier.

The parameterization of SAMBUCA relies on field sampling of the optical properties of the water body of interest. When this is not possible, the semi-analytical model can be parameterized with appropriate values from the literature. Based on the field data for the two sites, SAMBUCA was configured to estimate the concentrations of optically active constituents in the water column (Chl *a*, CDOM, and NAP), water column depth, and benthic substratum composition that produces the best fit between modeled and measured r_{rs}. These five environmental parameters are solved for on a pixel-by-pixel basis.

Processing of MB image data with SAMBUCA

The parameterization of SAMBUCA for MB was based on the field data acquired in July and August 2004 (see Table 1). The bottom albedo was expressed as the linear combination of every possible pair of benthic endmembers (see Table 4). In this context "endmembers" represent individual, homogeneous benthic or substrate cover types. The optimization ranges for the chlorophyll, CDOM, and NAP concentrations were wider than the ones applied by (Brando et al. 2009) in the deeper adjacent Rous Channel area in Moreton Bay to allow for conditions that were not characterized during the fieldwork such as sediment resuspension in very shallow waters and CDOM release by the submerged vegetation canopies as may occur in the shallow parts of the Rainbow Channel image.

Processing of LSI image data with SAMBUCA

To parameterize SAMBUCA for LSI the fixed values for seven SIOP scalar parameters (S_{CDOM}, S_{NAP}, a^*_{NAP} (440 nm), b^*_{bphy} (542 nm), $b^*_{b\text{NAP}}$, $Y_{\text{phy,}}$ and Y_{NAP}) as well the Chl *a* specific absorption spectrum $a^*_{phy}(\lambda)$ estimated in a coral reef environment at Heron Island, Australia were adopted (Wettle et al. 2004). The optimization ranges for the chlorophyll, CDOM, and NAP concentrations were estimated to cover the measured IOP ranges presented in Tables 1 and 3.

The environmental noise equivalent reflectance difference ($NE\Delta r_{rsE}$) is used in SAMBUCA to estimate the Substratum Detectability Index (SDI) as well as weighting function for the optimization residuum as it provides an integrated measure of sensor signal-to-noise ratio and scene-specific characteristics (Brando and Dekker 2003; Wettle et al. 2004). $NE\Delta r_{rsE}$ was estimated in the deepest waters in the CASI-2 and PHILLS imagery in the location identified as being the most homogenous using the methodology described by Wettle et al. (2004a).

Figure 4 shows that $NE\Delta r_{rsE}$ for the CASI-2 imagery is five times lower than the $NE\Delta r_{rsE}$ for the PHILLS imagery in the 500-700 spectral range. This difference is mostly due to the CASI-2 band-set design that optimized the signal-to-noise ratio (SNR) across the spectrum by using variable bandwidths. The bands in the blue and near infrared region have a bandwidth of ~20 nm, whereas the bands in the 500-680 nm range have a ~10 nm bandwidth. The PHILLS imagery has a 5 nm bandwidth across all of the spectral range. The LSI imagery is also affected by sunglint, whereas the MB imagery is not.

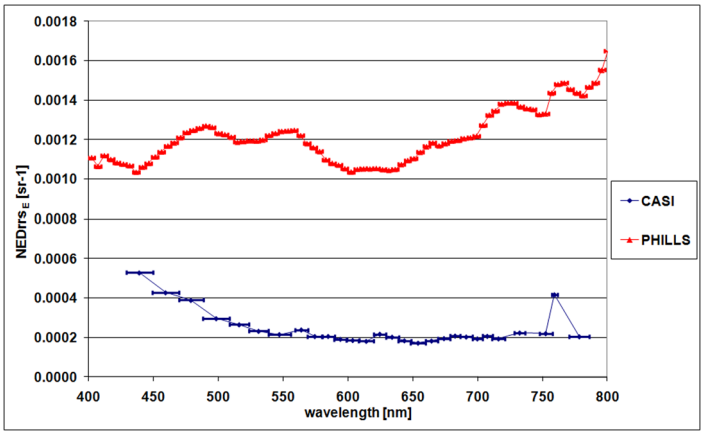

Fig. 4. The environmental noise equivalent reflectance difference (NEΔr_{rsE}) estimated in the deepest waters in the CASI-2 and PHILLS imagery using Wettle et al. (2004 **Q13**). The CASI-2 band-set has variable bandwidths, with blue and near infrared bands of ~20 nm, while the bands in the 500-680 nm range have a ~10 nm bandwidth. The PHILLS imagery has a 5-nm bandwidth across all the spectral range.

Comprehensive reflectance inversion based on spectrum matching and table lookup (CRISTAL)

The CRISTAL method for inverting R_{rs} (Mobley et al. 2005) is based on spectrum matching by searching through a precomputed database of spectra (Mobley and Bissett 2011). First, a database of R_{rs} spectra corresponding to various water depths, bottom reflectance spectra, water-column IOPs, sky conditions, and viewing geometries is assembled. This database is constructed using a special version of the HydroLight radiative transfer numerical model (Mobley et al. 1993; Mobley 1994) (www.hydrolight.info), which provides an exact solution of the unpolarized RTE for the given input. Each HydroLight-generated R_{rs} spectrum in the database is tagged by indices that identify the bottom depth, bottom reflectance spectrum, water IOPs (absorption, scatter, and backscatter spectra), sun zenith angle, etc. that were used as input to the HydroLight run. At a minimum, this database must contain R_{rs} spectra generated for environmental conditions close to those occurring in nature at the time and location where the image was acquired. The database also may contain spectra corresponding to environmental conditions much different from those of the image under consideration.

Second, the R_{rs} spectrum for a particular image pixel is compared with each spectrum in the database and the closest match to the image spectrum is found using a simple least-squares metric (Mobley et al. 2005). The environmental conditions in nature are then assumed to be the same as the input conditions that generated the closest-matching HydroLight-generated spectrum in the database. The CRISTAL-retrieved environmental conditions will always be one of the depths, ρ spectra, and IOP sets used to create the R_{rs} database. The CRISTAL technique does not do "dynamic" mixing of end members during image processing.

Finally, for example, the index tag identifying which bottom reflectance spectrum was used to generate the closest-matching HydroLight R_{rs} spectrum can be used to identify the bottom type at that pixel, or to obtain other information such as the bottom reflectance or IOPs at a particular wavelength. This process is repeated for each pixel in the image to generate corresponding maps of bottom depth, bottom type, or water-column IOPs. This inversion technique always results in a retrieval because there is always a closest matching spectrum, even if the match is poor. Thus there are no issues of failure to converge to a solution or of finding a local rather than a global minimum, as can occur in some iterative inversion techniques. If the database contains spectra representative of the imaged environment, then good results are obtained (Lesser and Mobley 2007; Mobley et al. 2005). However, as will be seen, if the database does not contain R_{rs} spectra corresponding to the environment in an image, then the CRISTAL technique is likely to provide a poor retrieval.

Database construction for CRISTAL implementation

An R_{rs} database for use with the LSI image was created as follows. For bottom reflectance spectra (ρ) mixtures of the clean ooid sand and the biofilmed sand end members were created by 20% steps, i.e., 20% clean sand + 80% biofilmed sand, 40% clean sand + 60% biofilmed sand, etc. The same was done with the biofilmed sand and the dark sediment. Mixtures of the bright and dark corals, and mixtures of the average turf and average macrophyte spectra, were created by 25% steps. Mixtures of the biofilmed sand and the average sea grass end members were created by 10% steps. Various mixtures of biofilmed sand and corals, e.g., 80% sand, 10% bright coral, and 10% dark coral were created. Finally, various mixtures such as 30% sand, 5% bright coral, 5% dark coral, and 60% turf algae were created. This gave a total of 39 end member and mixture bottom reflectances.

For the IOPs, mixtures were created by interpolating between the high and low sets of a and b by 25% steps. This gives five sets of a and b spectra. For each of those, backscatter spectra were created from the total scatter spectra using particle backscatter fractions of 0.01, 0.02, 0.03, and 0.04. This then gives 5 × 4 = 20 sets of IOPs, plus pure water, for a total of 21 sets of IOPs. This interpolation between the high and low a and b end member values means that the retrieved a and b will be correlated, i.e., a retrieval of high (low) absorption will also have a retrieval of high (low) total scatter. As will be seen, this oversimplification of nature proves to be adequate for LSI waters.

Bottom depths were set at 0.01 m, then by 0.25 m increments between 0.25 and 15 m, then by 0.5 m increments down to 25 m, plus 30 and 50 m, and infinity (optically deep water, for which the bottom reflectance is irrelevant). This gives a total of 84 depths.

These 39 bottom reflectances, 21 IOPs, and 84 depths give a total of 21× (39 × 83 + 1) = 67,998 R_{rs} spectra. The specialized HydroLight runs needed to generate nadir-viewing R_{rs} spectra

at 5 nm increments from 402.5 to 747.5 nm took about 45 h on a 2-MHz personal computer. Although this R_{rs} database generation is computationally expensive because the RTE must be solved for each combination of inputs, it needs to be done only once. Subsequent image processing is fast.

For the MB image inversion each of the 7 MB biota end members were mixed with the white sand and dark mud spectra by 20% increments, e.g., 20% white sand and 80% *Zostera muelleri*, 40% white sand and 60% *Zostera muelleri*, etc. Similar 20% increment mixtures were taken of white sand and brown mud, as well as a 50% to 50% mixture of light brown mud and dark brown mud. This gave 71 ρ spectra in all, counting the end members.

The absorption a and backscatter b_b end member spectra for MB were splined to the CRISTAL database wavelengths of 402.5 to 747.5 by 5 nm increments. Mixtures of these two end members were then created by 10% steps, for a total of 11 different a and b_b spectra. Because there were no data on the scattering coefficient, b spectra were obtained from the b_b spectra assuming particle backscatter fractions 0.01 and 0.03. This gave 2 b spectra for each combination of a and b_b spectra. Including pure sea water then gave a total of 23 combinations of a, b, and b_b. As with the LSI IOPS, this simple interpolation between the high and low a and b_b end member values means that the retrieved a and b_b will be correlated, i.e., a retrieval of high (low) absorption will also have a retrieval of high (low) backscatter. Although expedient for R_{rs} database creation, this oversimplification of MB IOPs proved to be inadequate for the MB image, as will be seen in the results section.

Bottom depths were placed at 0.01, 0.25, 0.50 . . . (0.25 intervals to) . . . 9.75, 10.0 m, and at infinity. This gives a total of 42 possible depths for the retrieved bathymetry. The 71 bottom reflectances, 23 IOPs, and 42 depths (41 depths plus one as infinity) give a total of $23\times(41 \times 71 + 1) = 66976$ R_{rs} spectra. The HydroLight runs needed to generate the nadir-viewing R_{rs} spectra took about 135 h on a 2-MHz personal computer. Although about the same number of R_{rs} were created as for LSI and the deeper bottom depths were omitted, the run time was longer because the IOPs were generally much greater, so that the optical depths, hence the time required to solve the RTE, were much greater in many cases.

Processing of LSI image data with CRISTAL

The CRISTAL-retrieved environmental conditions must always be one of the depths, ρ spectra, and IOP sets used to create the R_{rs} database. For LSI, the only preprocessing on the image data were subtracting 0.003 sr^{-1} from each image R_{rs} spectrum to improve the atmospheric undercorrection mentioned previously. Although some pixels were obviously contaminated by sunglint, no attempt was made to correct for the glint. The reason was that glint correction often invalidates pixels at depths less than 1 m deep, where the glint algorithm confuses bottom reflectance contributions to NIR R_{rs} with glint contributions in deeper waters. Removal or correction of glint-contaminated pixels would likely improve the CRISTAL retrieval statistics in the present comparison, for which the available acoustic data are at depths of 3 m or more. However, spurious elimination of very shallow pixels would be detrimental to many applications of CRISTAL and therefore is not done.

The CRISTAL spectrum-matching software automatically interpolates the 70 database wavelengths to the image wavelengths in the 402.5 to 747.5 nm range. Thus the spectrum matching was done at the 72 PHILLS bands. Each of the nonland pixels was processed independently by comparing the image spectrum with all of the spectra in the database to find the closest match using a least squares metric (Mobley et al. 2005). All wavelengths were weighted equally.

Processing the LSI image required 23 minutes on a 2 GHz PC. This required comparing 67,998 R_{rs} spectra for each of the 396,033 non-land pixels, or about 2.7×10^{10} spectrum comparisons in all. Thus the CRISTAL spectrum matching code was evaluating almost 20 million possible matchings per second. The processing times per image pixel are given in Table 5.

Table 5. Radiative transfer equation inversion methods processing comparison for each site and method: processor type/speed; time required to preprocess image and other data to run methods (not including image corrections); processing time; and average processing speed in terms of number of pixels processed per second.

Algorithm	Site	Processor	Pre-processing time	Image processing time	pixels processed per second	Program Code
HOPE	LSI	2.66 GHz		48 mins	156.39	C
HOPE	MB	2.66 GHz		90 mins	157.01	C
BRUCE	LSI	2.40 GHz		12 hours	10.43	C++
BRUCE	MB	2.40 GHz		15 hours	15.70	C++
SAMBUCA	LSI	*		1147 hours*	0.11	IDL/ENVI
SAMBUCA	MB	*		628 hours*	0.38	IDL/ENVI
CRISTAL	LSI	2.00 GHz	45 hrs	23 mins	326.38	Fortran95
CRISTAL	MB	2.00 GHz	135 hrs	22 mins	642.32	Fortran95
ALLUT	LSI	3.00 GHz	4 mins 12 s	2hrs 2 mins	61.53	C++
ALLUT	MB	3.00 GHz	6 mins 48 s	2hrs 32 mins	92.97	C++

* The actual processing was run over 16 processors –thus actual time was 3-4 days.

Processing of MB image data with CRISTAL

For the MB image data, the following preprocessing was performed: The MB image file contains nondimensional irradiance reflectance spectra just below the sea surface, R(0-). These spectra were converted to R_{rs} just above the sea surface (as used by the CRISTAL spectrum matching code) using Eq. 19. Other than this conversion of R(0-) to R_{rs}, no other manipulation of the image spectra was done.

The CRISTAL spectrum-matching software automatically interpolated the LUT standard wavelengths to the CASI image wavelengths in the 402.5 to 747.5 nm range. Thus the spectrum matching was done at the 25 CASI bands between 439.3 and 732.5 nm. Processing the MB image required 22 min on a 2-GHz personal computer.

Model inversion by adaptive linearized look-up trees (ALLUT)

The adaptive linearized look-up tree algorithm (Hedley et al. 2009) is an approach to facilitate spectral matching inversion of any radiative transfer models parameterized by a set of real-valued and integer parameters. The method used here is identical to that described in Hedley et al. (2009), but in addition, includes a local linear gradient calculation. In contrast to using predetermined parameter value steps to populate the LUT, as used by the CRISTAL approach, ALLUT construction proceeds by adaptively subdividing the parameter space to maintain an approximately evenly sampled spectral space. No a priori decisions on parameter discretization are required other than upper and lower bounds, the final distribution of parameter values in the ALLUT is dictated by the distribution of their corresponding modeled remote sensing reflectance vectors in spectral space. For example, regions of the ALLUT representing deep water will have comparatively fewer entries and larger parameter value steps for parameters of depth or benthic composition because these parameters have less effect on above water reflectance in deeper water. The recursive parameter subdivision leads to a tree-like structure that enables fast spectral matching of the above water reflectance by branch-pruning search algorithms. As a final optimization, the look-up tree is locally linearized, so that in addition to a point-wise table of parameter values and modeled reflectances, the gradient of reflectance in spectral space is calculated at each entry based on the adjacent LUT points. That is, for each tabulated spectral reflectance the ALLUT also stores a Jacobian matrix describing the linear slope of the mapping from parameter space to spectral space at that point. This matrix is determined by a least squares fit to the adjacent points in parameter space. Instead of matching reflectance spectra to the tabulated spectra, their distance to the slope sub-space is evaluated by least squares projection (Strang 1988) if they lie within the corresponding voxel of the table (Hedley et al 2009). Essentially, the mapping from parameter space to spectral space is represented by a series of linear segments rather than a set of points.

For analysis of the LSI and MB images, two variants of the semi-analytical model (Lee et al. 1999) were used as the forward model basis of the ALLUT construction, for the LSI image the original formulation of the HOPE model was used whereas for the MB image, because SIOPs were available, the SAMBUCA model was employed. In both cases a pair-based benthic endmember model for bottom reflectance, ρ, was used in which, identically to SAMBUCA, the ALLUT contains entries based on every possible pair of benthic endmembers in a linear mix according to a parameter, $0 \le P \le 1$. The ALLUT therefore differs from the other semi-analytical approaches here primarily in the inversion method, whereas the solution returned is global, and so not subject to any convergence of local optima issues of successive approximation, it is subject to a residual discretization error due to imperfect representation of the forward model by the ALLUT.

Processing of MB and LSI image data with ALLUT

The input parameter ranges for the two semi-analytical forward models used to process the LSI and MB images are given in Table 3. For the LSI image, where Lee et al. (1999) formulation requires that the Y parameter, the particulate backscatter slope, be estimated by a preprocessing step on a pixel-by-pixel basis, however because the ALLUT must be precalculated and also to reduce the degrees of freedom in the model Y was fixed based on the mean calculated over the image according to the equation given in Lee et al. (1999).

In addition, the semi-analytical model contains a conversion from sub-surface remote-sensing reflectance, r_{rs}, to above surface remote sensing reflectance, $R_{rs} = \zeta r_{rs}/(1 - \Gamma r_{rs})$ where Lee et al. (1999) estimated $\zeta = 0.5$ and $\Gamma = 1.5$ by regression over many runs of HydroLight with their input data set. In the ALLUT construction for the MB image processing the value of ζ used instead was 0.55. This was estimated from multiple runs of PlanarRad, an open-source full plane-parallel RTE solver similar in design to HydroLight (and which has been validated against HydroLight and other RTE solvers [Hedley et al. 2009]). The value of $\zeta = 0.55$ gave a slightly better fit for the estimates of R_{rs} and r_{rs} computed from PlanarRad over the first 10,000 LLUT entries produced from the SAMBUCA model parameterized for the MB image (assumption Petzold's phase function, giving a backscatter fraction of 0.0183).

As for the other methods, spectral matching was conducted with even weighting over the 400-750 nm range (72 bands for LSI, 25 bands for MB). All spectra were resampled to the image bands before any processing was applied. Processing was conducted on a standard desktop computer, where the primary limitation was available computer memory, because the construction and search algorithms require that the entire ALLUT must fit into the memory at once. The machine used had 8 Gb memory, which allowed the LSI ALLUT to contain 2 × 106 entries, whereas the MB ALLUT could be larger, because the spectral data have fewer bands and contained 5 × 106 entries. The times for ALLUT construction and image processing are given in Table 5. The primary computational cost in the spectral matching search algorithm is the least squares projection onto the local linear gradient function. In comparison, a stan-

dard point-wise look-up over the 5 million pre-calculated spectra, as described in Hedley et al. (2009), processes the MB image in less than 3 min, but the retrieved parameter values are potentially subject to greater discretization errors.

Evaluation and intercomparison procedures

Evaluation of the different methods for deriving bathymetry, optical properties, and benthic composition, focused on measurement of absolute and relative accuracies of the derived parameters in relation to the reference field data sets, and on comparison of their relative performance in terms of required time and computation resources. This was to address the following five points: (1) accuracy and processing time of each mapping algorithm; (2) conditions under which existing mapping models do and don't work; (3) the adaptability of mapping models to two different locations and two imaging sensors; (4) recommended products and procedures for mapping in optically shallow waters; and (5) international best science practice.

Direct assessments were able to be made for depth retrievals, while more indirect assessments of accuracy were made for optical properties, in terms of spectral absorption, backscattering, and reflectance. As limited benthic composition information were available in a suitable reference data format, the different output reflectance products for each site were subject to the same image classification routine, and the resultant benthic composition maps were compared.

Bathymetry

Validation of retrieved bathymetry was performed by matching boat-based acoustic survey data for each site to the depth values retrieved for the imaged areas, ensuring the data were accurately co-registered at a pixel level, then extracting retrieved bathymetry from the image at each suitable acoustic depth survey point. This generated > 3500 points for LSI and 163 points for the MB image subsets. An IDL routine was used to plot the acoustic and retrieved bathymetry and then measure coefficient of determination (R^2) and root mean square error to provide a visual and quantitative assessment of the nature and strength of co-variation, and the range(s) of depths over which the SA and LUT retrievals worked. The use of standardized scatter-plots and scaled RMSE and R^2 values made it possible to compare the relative performance of each algorithm within and between sites.

Optical properties

Validation and intercomparisons of optical properties retrieved by each algorithm at each site presented more of a challenge, due to the difficulty in obtaining exact match-ups in time and location, between image and in-situ measurements of the same property. The optical properties selected for comparison were a440 nm and b_b555 nm and ρ 555 nm, from a series of selected targets at each study site. To extract representative a440 nm, b_b550 nm, and ρ555 nm values, polygons were placed over a range of water depths and benthic cover types at the LSI and MB sites. This produced 45 polygons at each site, with approximately 9900 pixels in LSI and 3300 in MB. The resulting a440 nm, b_b550 nm, and ρ555 nm values produced by each of the five SA or LUT methods were then extracted from each polygon and plotted as frequency histograms to provide a visual assessment of the similarities in retrieved a440 nm and b_b550 nm values. No suitable in-situ a440 nm and b_b550 nm data were available to provide an absolute match-up and accuracy assessment. A similar approach was used to assess retrieved bottom reflectance at 555 nm values from each SA or LUT inversion. In addition, representative R_b spectral signatures across three benthic cover types were extracted from ROIs (regions of interest) for LSI and MB. As this parameter is not retrieved by the HOPE model, as it only estimates whether a pixel is sand or seagrass, it is not included in the plot.

Several other forms of assessment were conducted, and used for discussion amongst the intercomparison team during the preparation of this manuscript and are not reported directly here, but were used to support comparisons discussed in the text. The data used for these assessments came from a smaller set of polygons, 13 on LSI and 10 on MB, which were used to extract and plot the mean retrieved a440, b_b550 nm, and ρ555 nm at each of the polygons, allowing assessment of spatial variations in each inversion model's performance. Scatter plots, coefficients of determination, and least-squares quotients were also computed for the retrieved value from each inversion method and their group median parameter value. Image plots of a440 nm, b_b550 nm, and ρ555 nm values, and an RGB composite using B: 5 (516nm) G: 10 (584nm) R: 15 (634nm), were also produced for each site, from each of the inversion models used.

Benthic—Substrate reflectance and mapping

Benthic substrate reflectance and classification was only carried out for the Moreton Bay image because a lack of sufficient data from the LSI site did not allow a comparable level assessment. The aim of this section was to subject each of the R_{rs} images retrieved for MB from different inversion methods, to the same classification routine to map sea grass cover and composition, and then compare each sea grass cover and composition map to a reference data source and each other. A full description of the field data collection and analysis process to produce georeferenced photo-transects with percentage seagrass-composition and -species at each photo point can be found in Phinn et al. (2008) and Roelfsema et al. (2002). The 56 transects, with 2800 1.0 m × 1.0 m digital photographs at 2.0 m intervals along each transect covered 82% of the study area, but were limited to depths shallower than 3.0 m. These data were used to define polygons for training and validation sources to produce a seagrass cover and seagrass species composition map from the R_b image produced by each of the inversion methods except HOPE. Approximately 50% of the polygons were for training the supervised classification and 50% for validation, with the selection being stratified to cover a full range of seagrass cover and species in training and validation sites. The training signatures were gathered for % cover

and species as follows, seagrasscover classes: 0% to 10%, 10% to 40%, 40% to 70%, 70% to 100%; and species classes: *C. rotundata, S. isoetofoilum, Z. muelleri, H. ovalis, Z. muelleri /H. ovalis*, sand and deep water. The training sites were then applied to each R_b image using ENVI's Spectral Angle Mapper, classification routine with same input parameterization and decision rules, so that any variation in output classified images were due to differences in the input R_b image produced from each inversion method. Use of SAM as a classifier also provided a focus on differences in retrieved R_b spectrum shape, rather than magnitude.

The output seagrass cover class maps and seagrass species maps were validated against the 50% of polygons not used for training. This was done on a polygon by polygon basis to extract a number of pixels for direct comparison, and yield error assessment tables, along with overall and individual class accuracies for cover and species composition in the R_{rs} produced by each inversion method (Phinn et al. 2008). As the training and validation had all been conducted using the same field data set and methods overall and individual accuracies could be compared.

Assessment

For the two study sites assessed in this work, all five SA- or LUT-based inversion methods were able to estimate bathymetry, water column composition, and to map the presence and factional cover of specific benthic substratum and vegetation. However, the simultaneous retrieval of all these properties does mean that the accuracy of each estimated property is highly dependent on the retrieval results of each of the other properties. For example, benthic reflectance spectra can influence the bathymetry and water optical properties retrieval or a too small range of optical variables can influence bathymetry and benthic variable retrieval. The relative effects of each of these depends on water depth and clarity, so sometimes one parameter has a small effect; sometimes a large effect. The assessment below shows that relatively high absolute accuracies were obtained for bathymetry estimates across all methods, down to 8-13 m in both study sites. Realistic and comparable water IOP values were estimated from all algorithms for each of the two sites. For bathymetry, all SA and LUT inversion methods produced more accurate depth retrievals than the empirical approach by Lyzenga, which was confounded by dark benthic cover types.

The LUT-based approaches were fast but were sensitive to choices in discrete parameterization of the water column optical components for the look-up table generation. The SA inversion approaches can vary the water column optical property parameterizations in a virtually continuous manner. The HOPE, CRISTAL, and ALLUT methods were quicker and required less input, but did produce lower accuracy bathymetry and IOP values. Variations in the accuracy of all estimated parameters were related to variations in water depth, and the level of complexity or detail provided for parameterization of IOP and benthic reflectance. In turn, these factors also affected the relative performance of each SA and LUT inversion method, through differences in the complexity of the equations used in each method, in terms of representing bathymetry, IOP and numbers of benthic/substrate features, and the final retrieval approach. This produced a hierarchy of methods, ranging from least complex, HOPE and CRISTAL, to SAMBUCA, BRUCE, and ALLUT. The assessment section expands these conclusions, by analyzing and comparing retrieved bathymetry, IOP and then benthic cover maps, and concluding with an assessment on the main factors affecting processing time and accuracy.

Before discussing the results, it should be noted that in optically shallow waters the retrievals of water column IOPs, bathymetry, and substratum reflectances vary with depth. In areas with little water column attenuation, the water column contribution to at-surface reflectance is relatively small, and the substratum reflectance component is relatively large, thus giving greater certainty in the retrieval of bathymetry and bottom reflectance. In deeper waters, the water column contributes relatively more to the signal than the bottom reflectance, and thus the water column composition estimate becomes more accurate whereas the substratum and depth estimate become less accurate.

Bathymetry

The results of the bathymetry retrievals are shown in Fig. 5. The main conclusions from the comparison of the bathymetry assessments were that all inversion methods, with the exception of Lyzenga's empirical approach (Lyzenga 1978), are able to estimate depth in these optically shallow waters to about 7 to 13 m deep over multiple benthic and substrate cover types. The empirical approach was overall least accurate as its a-priori assumption is that the optically shallow waters have a uniform light or dark bottom color and that the water column is homogeneous.

Significant variations in estimated depths occurred when optically deep pixels were processed, e.g., beyond 10 m depth in the MB Rainbow Channel. Unless an inversion method has a built in method for assessing when a pixel is optically shallow or optically deep (e.g., SAMBUCA) the inversion method may incorrectly retrieve depth estimates. Although not automated, many of the inversion processes can also deliver information that the user can assess to estimate the water-column-to-substrate relative contributions to surface reflectance. Following similar methods to those adopted by SAMBUCA, and by selecting a threshold for water column versus substrate contributions to the surface reflectance, the user can then decide which pixels might be less or more accurate in terms of bathymetry retrievals.

Another reason for depth retrieval variations is the inversion model's IOP and R_{rs} end-member parameterization not being optimized to local environment or levels of variation. This is the reason the CRISTAL retrieval in MB was poor beyond 5 m depth. With better IOP parameterization of the

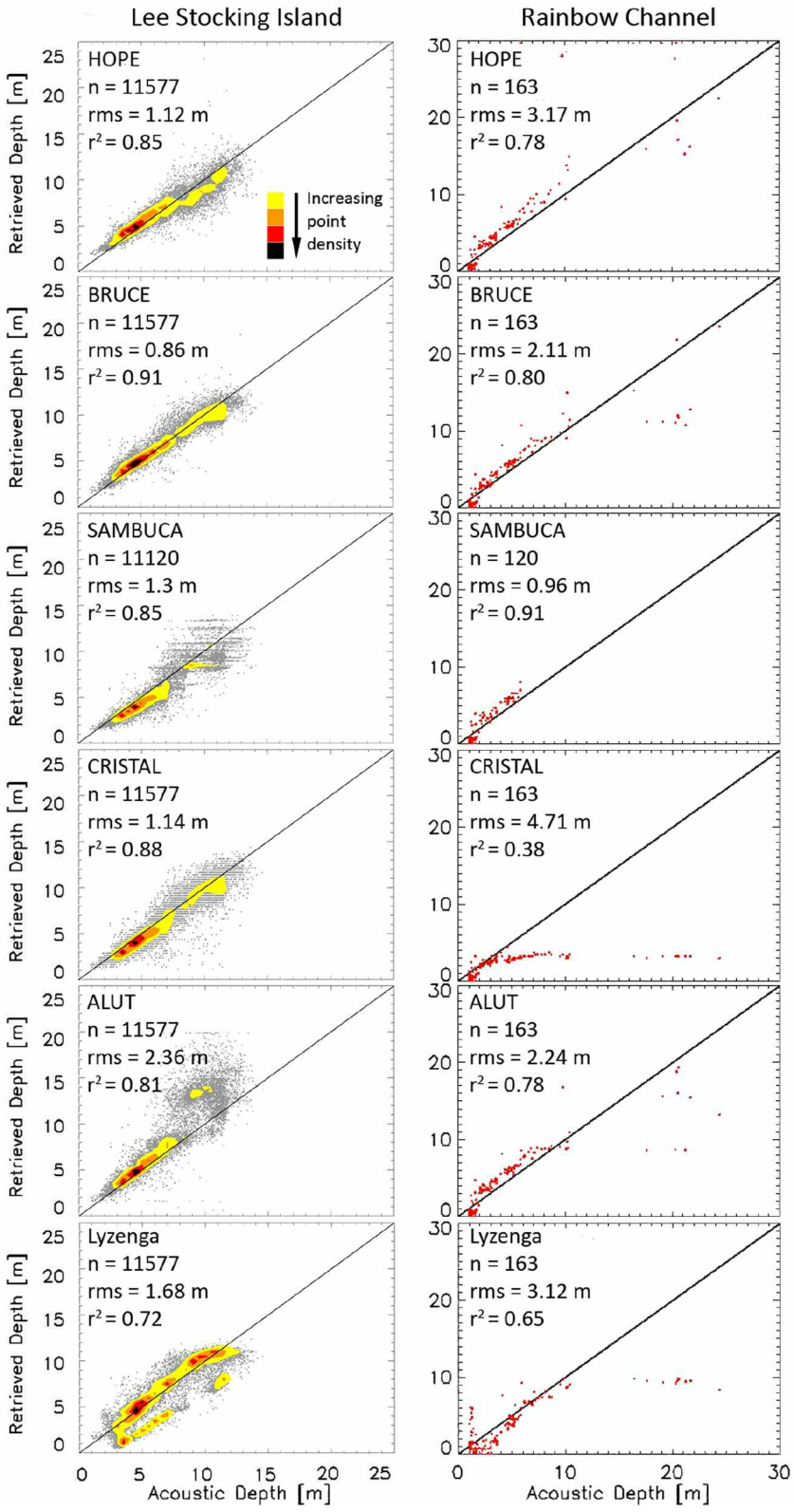

Fig. 5. Scatter plots and multi-variate statistics for retrieved and measured bathymetry along two transect lines for Lee Stocking Island-Horseshoe Reef and Moreton Bay-Rainbow Channel for each of the five inversion methods and the Lyzenga (1978) approach. The SAMBUCA plots have fewer validation points (*n*) as the method has an inbuilt process for masking out optically/quasi-optically deep pixels and in the MB plot, this increases the R2 and lowers RMSE values as discussed in the "Bathymetry Assessment" section. Note the x-axis range differences between the right and left panels.

database, it is presumed that the CRISTAL would have performed significantly better.

Future application of the SA and LUT inversions should only provide bathymetry estimates at optically shallow pixels and classify optically deep pixels as such. This recommendation is valid in inaccessible areas too. Except for inaccessible areas it is recommended to focus on using the most representative IOP and R_b end-members. This may be enhanced by use of existing bathymetry or a priori knowledge of R_b variability or IOP ranges or SIOP and concentration ranges to constrain estimations of bathymetry. For inaccessible areas those codes that can approximate some of this information from the image spectra are most appropriate such as HOPE. An example of the type of output bathymetric map produced by the ALLUT approach is shown in Fig. 6a for the Moreton Bay image. For both the LSI and the MB images, Fig. 5 shows all the bathymetry retrievals in scatter plot form and Fig. 7 shows comparisons of measured and retrieved depths along two acoustic survey lines.

Overall, most results were accurate from 0–13 m in LSI and 0–10 m in MB, with differences between the approaches evident in the variations of estimated depths, as indicated by RMS values, and the depth(s) below which the retrieved depth deviated significantly from actual depth.

For the LSI image, the retrievals ranged from a RMS error of 0.91 m for the BRUCE method to 2.36 m for the ALLUT method and for the MB image the retrievals ranged from a RMS error of 0.96 m for the SAMBUCA method to 4.71 for the CRISTAL method.

In the Moreton Bay image, SAMBUCA was the only algorithm to deal with the transition from optically shallow to optically deep water at around 10 m. The SAMBUCA method flagged pixels beyond 7 m as optically quasi-deep or as optically deep, and therefore did not estimate bathymetry, hence the smaller number of pixels, low RMS, and higher R^2. However, this sophistication comes at some cost to processing speed as these calculations are performed for every pixel in the image.

The look-up table based bathymetry retrievals (CRISTAL and ALLUT) for LSI (Fig. 5) were comparable to those by the HOPE, BRUCE, and SAMBUCA algorithms. This indicates that

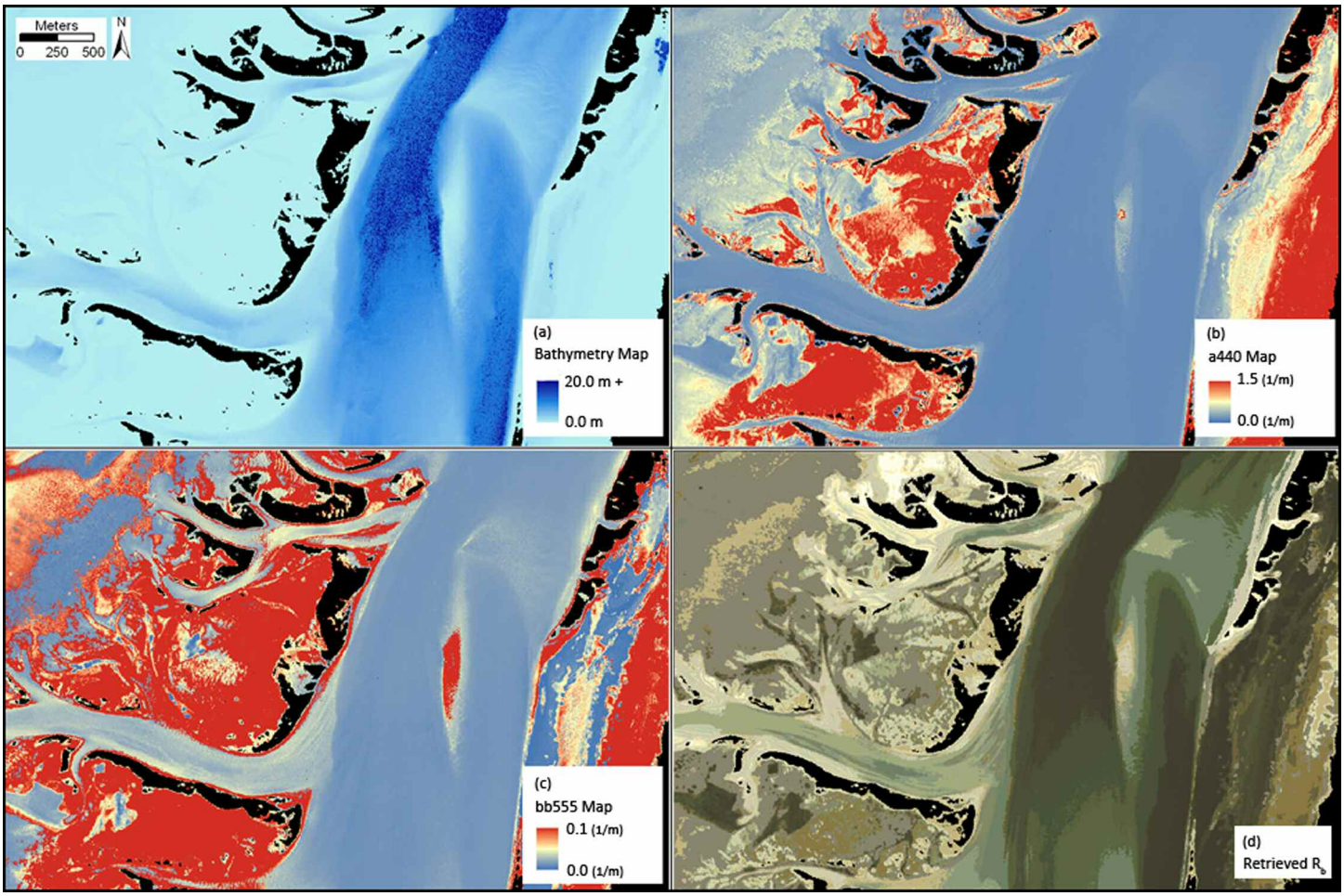

Fig. 6. Example output images from Moreton Bay-Rainbow Channel showing retrieved parameters from the ALLUT method for (a) bathymetry, (b) a440 nm, (c) b_b555 nm, (d) bottom reflectance, R_b, in blue green and red bands.

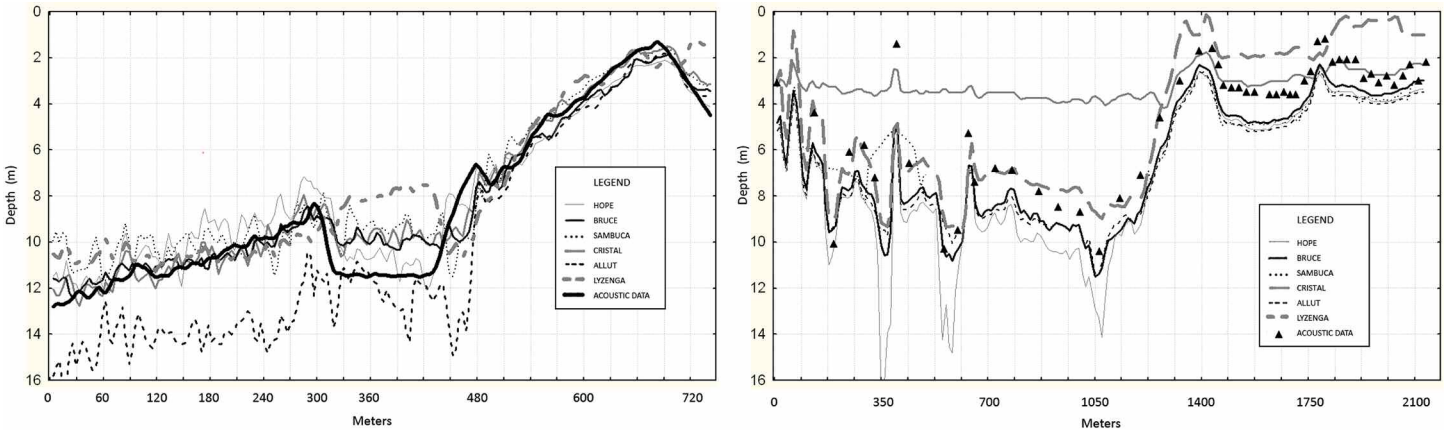

Fig. 7. Comparative plots of measured and retrieved bathymetric cross-sections from the (a) Lee Stocking Island-Horseshoe Reef and (b) Moreton Bay-Rainbow Channel images, taken along the A-B transects shown in Fig. 1.

all SA and LUT approaches captured the relevant physics of the RTE in modeling R_{rs} and the environmental conditions in the LSI image. Much of the common spread in the retrieved depths may be due to the imperfections of the LSI image itself, namely the pixels contaminated by sunglint, pixels with poor radiometric calibration or atmosphere correction, and mismatches between acoustic sounding locations and image pixels because of imperfect geolocation. The potential for these other factors needs to be assessed.

The retrieved bathymetry across transects with in situ acoustic depth data in Fig. 7 shows how the different methods behave, for the Lee Stocking Island and Moreton Bay. For LSI from 0-300 m along the transect all methods (except for ALLUT) follow the depth from about 13 m to 9 m quite well. ALLUT overestimates depth quite severely from 0 to 480 m. The LSI feature from 300 to 480 m at a depth of 11.5 m posed a problem for most inversion methods with the HOPE method giving the most accurate results and Lyzenga the worst. After 480 m through to 720 m, all methods estimated bathymetry quite well. BRUCE, SAMBUCA, and Lyzenga all are able to follow the acoustic data with a slight overestimation of depth.

For the MB transect CRISTAL underestimates depth significantly due to its poor a priori parameterization choices—although it is the best performer in the shallow areas above 4 m depth from 1300 m to 2200 m along the transect. The Lyzenga method follows the acoustic depth measurements closely between 4 and 8 m depth. At 350 m in the MB transect a shallow feature occurs according to the acoustics, all inversion methods do record a shallow feature there, but not very accurately. As the acoustics have a geospatial error as well as the imagery and this feature is quite small, it may negatively influence these accuracy estimates.

The HOPE method is the simplest version of the semi-analytical based forward and inverse models, with a fixed a priori parameterization and using only two benthic reflectance spectra (sand and grass). The results of the HOPE method are above average for LSI. They appear as below average quality for MB for bathymetry retrievals in Fig. 5, but with removal of the three to four outlying deep points, HOPE produces above average depth retrievals. Similar fine-tuning can occur in the other algorithms, although SAMBUCA does this automatically and objectively (note the reduced N in Fig. 5).

The SAMBUCA method performed well for bathymetry in MB as it deals intrinsically with the conversion from optically shallow to optically deep waters. This also means it is probably one of the most suited methods for dealing with turbid water environments. SAMBUCA performance was similar to HOPE for LSI. Across LSI and MB, BRUCE had the lowest RMS of 0.86 m. It is informative to compare the MB results for all methods for depths less than 7 m (the depth at which SAMBUCA defines the water column to be too deep for accurate bathymetry retrievals). In this depth range HOPE, BRUCE, SAMBUCA, and ALLUT all appear comparable.

The BRUCE method performs well for estimating bathymetry for the LSI image. This may be due to (1) the image preprocessing applied that ensures sunglint and residual atmospheric correction effects are reduced; and (2) use of a three component benthic reflectance fractions estimation.

The Lyzenga method produced a wide range of estimated depths for actual depths, as it assumes only one R_b type in its implementation in this paper. Previous approaches addressed this limitation by segmenting images into different bottom types and developing separate depth models with unique R_b values for each and combining the output bathymetric surfaces (Green et al. 2000).

Water column optical properties

Establishing direct assessments of error of retrieved water column optical properties, in terms of matching in-situ and retrieved parameters was difficult due to a lack of concurrent in-situ data. Figs. 6b and 6c show examples of a440 and b_b555 for MB derived by the ALLUT method. Figure 8 illustrated that each method retrieved similar ranges of IOP values, which were within the range of previously collected in-situ IOP data, especially over deeper water bodies. The CRISTAL approach

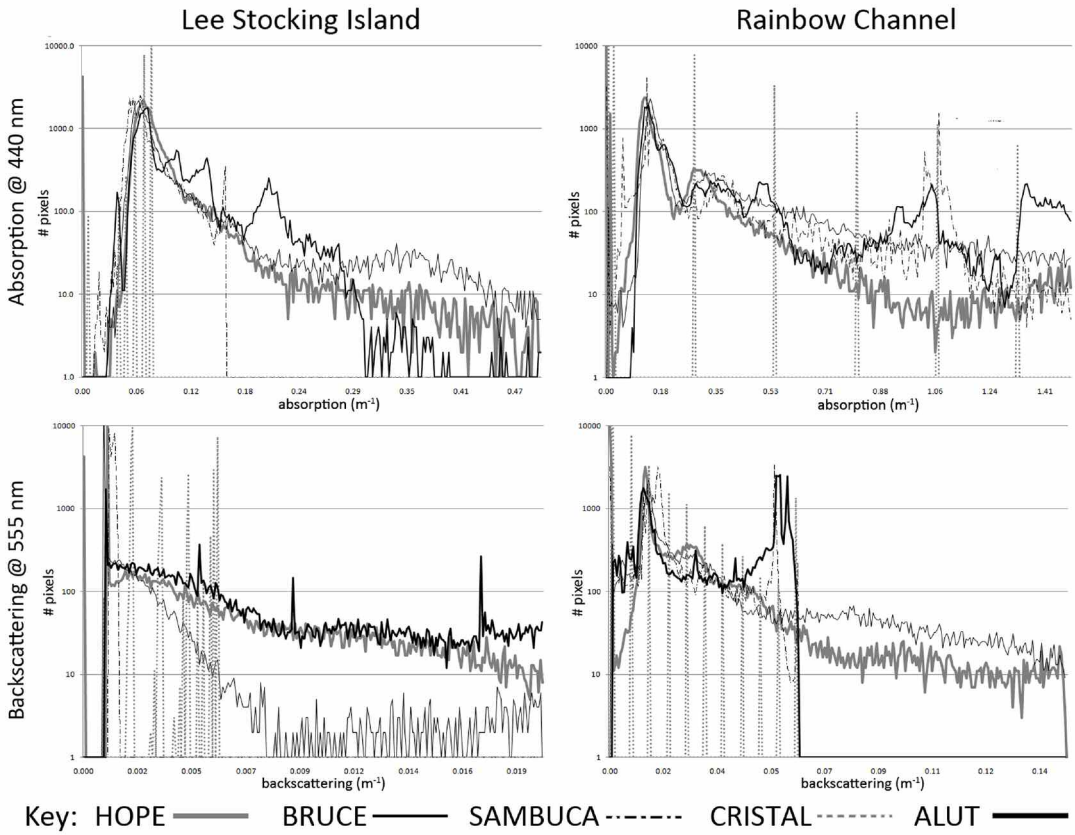

Fig. 8. Frequency histograms of estimated a440 nm (top row) and b_b555 nm (bottom row) pixel values from each of the inversion methods in the Lee Stocking Island-Horseshoe Reef and Moreton Bay-Rainbow Channel images.

did provide different distributions of retrieved a440nm and b_b555nm, as it assigned data to discrete classes, rather than a continuous range of data. Deviations between retrieved a440nm and b_b555nm in both the LSI and MB images may be due to water column depth effects, with retrieval of a water column composition having less signal to use in shallower areas with benthic reflectance signals dominating. Other deviations are caused by a priori parameterization choices for range or distribution of each algorithm.

Figure 8 shows the frequency distribution of retrieved total absorption at 440 nm for LSI and MB and the retrieved total backscattering at 555 nm for LSI and MB. Similar frequency distributions were retrieved by each method for both sites, with the most obvious difference being those values from the CRISTAL method which were binned into set ranges of a440 nm and b_b555 nm values. Both sites had limitations in establishing a direct match-up between retrieved water column optical properties and in-situ measurements.

The only ac9 data for LSI were taken either at the time of the LSI PHILLS overflight, but at a location about 1 km outside the image, or on a different day, but near the center of the image used in this study. Colocated, simultaneously acquired IOP measurements were not available for validation of retrievals at specific LSI image locations.

The available ac9 measurements show a440 values in the range of 0.05 to 0.06 m^{-1}, which is consistent with the most commonly retrieved values from all methods. This indicated that all inversion methods were able to recover realistic a440nm values for the LSI image. There is some variability in the distribution of values where the CRISTAL method had a limited number of discrete a440nm "classes," whereas most other inversion methods show a more gradual distribution across the 0.001 to 0.18 m^{-1} a440nm range. CRISTAL inversion values had a maximum a440 of 0.08 m^{-1}, SAMBUCA a maximum a440 of 0.16 m^{-1} (most likely due to some pixels being classified as optically deep), HOPE and BRUCE showed a more gradual decline of a440 at higher a440 nm values, The ALLUT inversion shows a few more pixels with values between 0.15 and 0.50 m^{-1} a440.

Although there were no match-up in-situ backscatter data collected for LSI, the available ac9 scattering coefficients were in the range of b555nm = 0.10 to 0.13 m^{-1}. The backscatter retrievals have a strong peak at b_b555nm = 0.0008, and except for HOPE and ALLUT few have pixels with b555nm values beyond 0.006 m^{-1}. These values are consistent with the measured b and an assumed backscatter fraction of 0.01 (i.e., b_b555nm values between 0.0010 to 0.0013 m^{-1}). Only the CRISTAL retrievals show b_b555 values corresponding to higher backscatter fractions in discrete bands up to 0.006 m^{-1}.

For the MB image, more information on potential match-up IOP values was available. Most of the retrieved a440nm values cluster between 0.1 and 0.25 m^{-1}, which is at the low end of the MB IOP end members (measured a440nm for all of MB ranged from 0.025 to 2.63 m^{-1}). Note that the most commonly retrieved CRISTAL values are the two lowest in its database. The HOPE and SAMBUCA models also had many pixels retrieved at very low values. The CRISTAL inversion method shows discrete peaks in distribution associated with its a priori choice of allowed ranges and intervals in a440nm. Between a 440nm of 0.8 and 1.5 m^{-1}, all methods show varying frequency of a440nm values.

The bulk of retrieved b_b555nm values for MB fall between 0.005 and 0.06 m^{-1} for all inversion methods and between 0.055 and 0.063 m^{-1}, with HOPE and BRUCE the only models also producing b_b555nm values greater than 0.06 m^{-1}. Other methods have applied processing constraints to limit the range of output values. There was significant difference between b_b555nm values from 0.045-0.06 b_b555nm. All inversion methods had many pixels with very low b_b555 values, below 0.002 m^{-1}.

Two factors may explain some of the observed variance in retrieved pixel values for a440nm and b_b555nm, in relation to water depth and algorithm parameterization. In relation to the first factor, the fraction of upwelling radiance from the interactions of photons within the water column becomes less, compared with the fraction derived from the substratum, as the water column gets shallower and vice versa. As a consequence of this effect, values of absorption and backscattering of the water column become less reliable as the water column is shallower, whereas the benthic reflectance contribution becomes larger, hence retrievals in shallow waters, such as most of the MB image, which is < 3.0 m depth, may be less accurate. For the second factor (algorithm parameterization), some of the choices made in simplifying and parameterizing the inversion methods can also play a role in very shallow areas. These points suggest that the most accurate values for a440nm and b_b550nm are to be derived from optically deep parts of water-bodies in the imaged areas. The automated masking of optically deep pixels carried out by SAMBUCA removes these deep water results from its delivered products.

The five inversion methods varied considerably in their initial parameterization for optical water column properties, mainly in terms of using discrete class intervals to simplify processing (CRISTAL) or a continuous range and distribution of values. Table 3 summarizes these parameterizations as well as the ranges used for each IOP. The HOPE method uses an a priori fixed IOP parameterization and the BRUCE method parameterizes water column IOP from the image reflectance itself; SAMBUCA parameterizes using regional optical knowledge and sets knowledge based boundaries on permutations. The CRISTAL method requires a priori choices to be made for creating the database, which end up being a choice for certain discrete intervals in optical water variables. The ALLUT approach is a hybrid of all these approaches as indicated by its parameters in Table 3, which were similar to HOPE, BRUCE, and SAMBUCA.

Benthic—substrate reflectance and mapping

The aim of this activity was to assess the accuracy of the retrieved R_b values from each of the inversion methods. The results presented must be considered in the light of the depth limitation of the validation data from 0 to 3 m deep for Moreton Bay only, whereas the inversion methods all worked to about 10 m deep. Thus conclusions reached here may not apply to inversion results beyond 3 m depth.

Two approaches were used to assess the accuracy of the retrieved R_b values between almost zero depth and 3 m depth, and neither were optimal in terms of a providing a direct spatio-temporal match between pixel-based R_b estimates and coincident R_b measurements. The first approach compared in-situ field spectrometer R_b measurements of the most commonly occurring benthic cover and substrate types with sites known to contain these in the retrieved R_b images for LSI and MB. The second approach used the retrieved R_b images from each method from the MB site, subjected them to the same image classification routine to produce two maps: (1) four classes of seagrass percent cover and (2) benthic cover and substrate types. Error matrices (available on request) and accuracy measures were produced from each of the maps, for each inversion method, by using a published seagrass cover and benthic cover types from the same MB image data (Phinn et al. 2008; Lim et al. 2009). As the output of the inversion methods differs significantly between a simple binary choice of mainly sand or mainly seagrass (HOPE), to more sophisticated estimates of either the most dominant substratum, or a combination of the two most likely substratum types per pixel (SAMBUCA), or a combination of the three most likely substratum types per pixel (BRUCE), or a pre-determined choice of substratum combinations for a LUT creation (CRISTAL) direct quantitative comparisons were not possible.

The retrieved R_b values for selected benthic features from both LSI and MB for each inversion method are shown in Fig. 9. For the LSI image, all inversion methods retrieved values matching the shape and magnitude of in-situ field spectrometer measurements for seagrass, however only ALLUT matched the coral R_b spectra and all methods underestimated clean white sand. Slightly worse results were observed for the MB image for each benthic-substrate cover type. For both sites, with the exception of ALLUT, no method reproduced reflectance peaks and troughs associated with seagrass.

A more accessible assessment of the differences between the inversion methods for estimating R_b values was provided by visual and classification analysis of each of their output R_b images. Visual assessment of true color composite images, such as that shown for the ALLUT method in Fig. 6d in comparison to the original image (Fig. 1), provide a quick and qualitative assessment of the precision (radiometric range) and accuracy (reproduction of all imaged features). The inversion methods

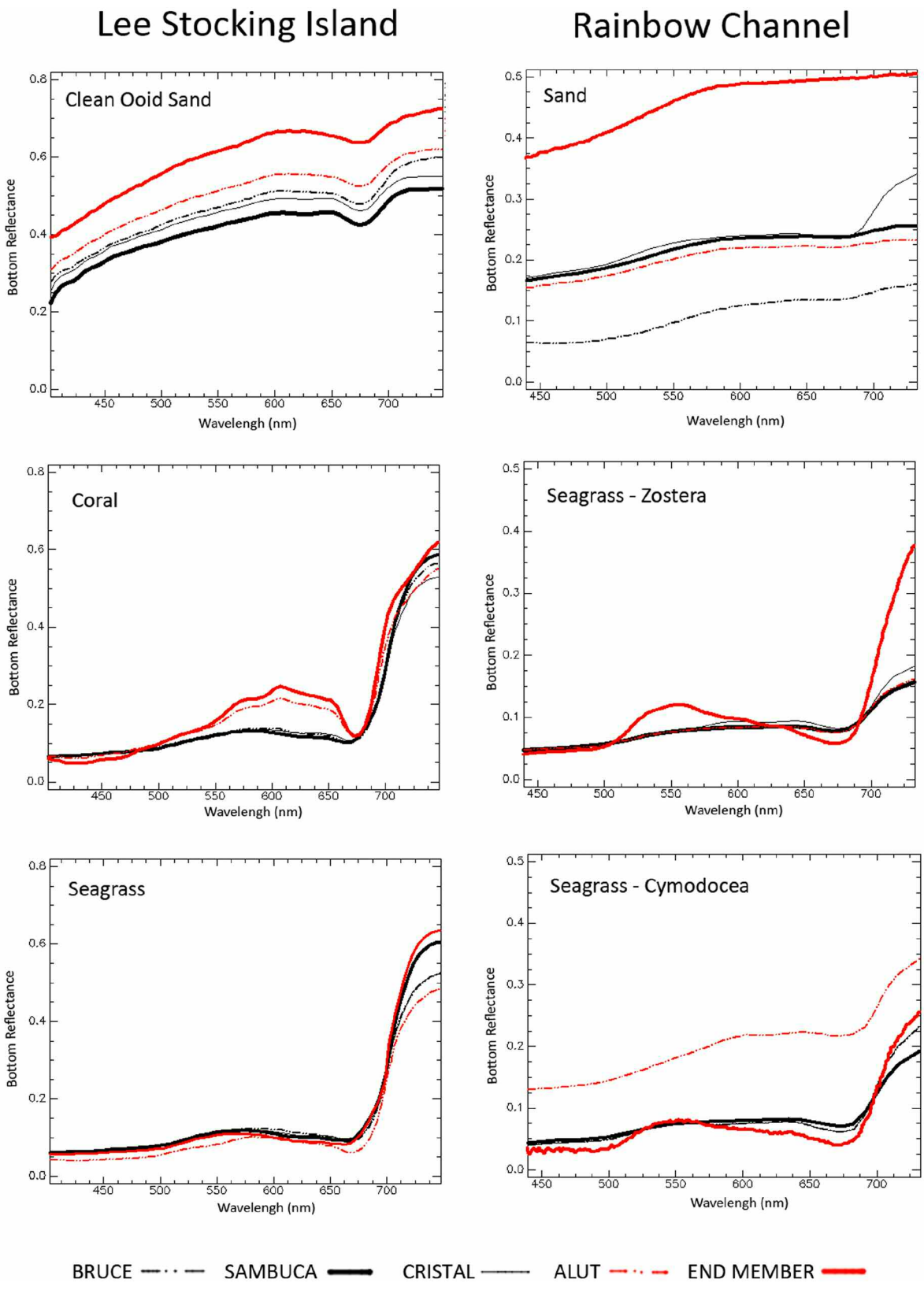

Fig. 9. Representative R_b spectral signatures across three benthic cover types extracted for Lee Stocking Island-Horseshoe Reef and Moreton Bay-Rainbow Channel, from the retrieved R_b image produced by each approach. Note there is no retrieval for the HOPE model, as it does not create an R_b spectrum (either directly from a spectral library or through combining spectra) and only estimates whether a pixel is sand or seagrass.

using less endmember reflectance spectra in each pixel appear to be level-sliced or classified as true-color images, lacking the full radiometric precision of the original scene. Comparison of the seagrass-cover and benthic-substrate cover classification maps and error matrices provided similar results with more quantitative measures of differences (Fig. 10). Both the output seagrass cover classification and benthic-substrate cover maps provide similar assessments to the visual analysis of true color R_b images, with those methods that allowed more detailed representations of benthic features making up a pixel (e.g., ALLUT and BRUCE) producing maps that more closely resembled the reference maps. The overall accuracy figures confirm this visual assessment, with seagrass cover overall accuracies of: reference = 89%, ALLUT = 79%, BRUCE = 84%, CRISTAL = 83%, and SAMBUCA = 59%; and benthic-substrate cover overall accuracies of reference = 89%, ALLUT = 78%, BRUCE = 79%, CRISTAL = 65%, and SAMBUCA = 52%. In all inversion methods, lower individual class accuracies were associated with low covers sites (<40%) and mixed benthic-cover zones. Those inversion methods that allowed more detailed representations of benthic features making up a pixel to estimate values, exhibited lower classification accuracies in mono-specific areas not represented by their endmembers. This benthic reflectance comparison exercise was limited to depths of 3 m. Future comparison studies would benefit from a more rigorous in situ campaign of collecting a representative benthic reflectance, as well as validation data from depths right down to the maximum of substratum visibility, which should have been about 10 m depth for this part of Moreton Bay. GPS-based mapping of polygons, preferably three times larger than the remote sensing pixel size, of homogenous areas of substratum and benthic cover would significantly aid in comparing and improving methods of inversion.

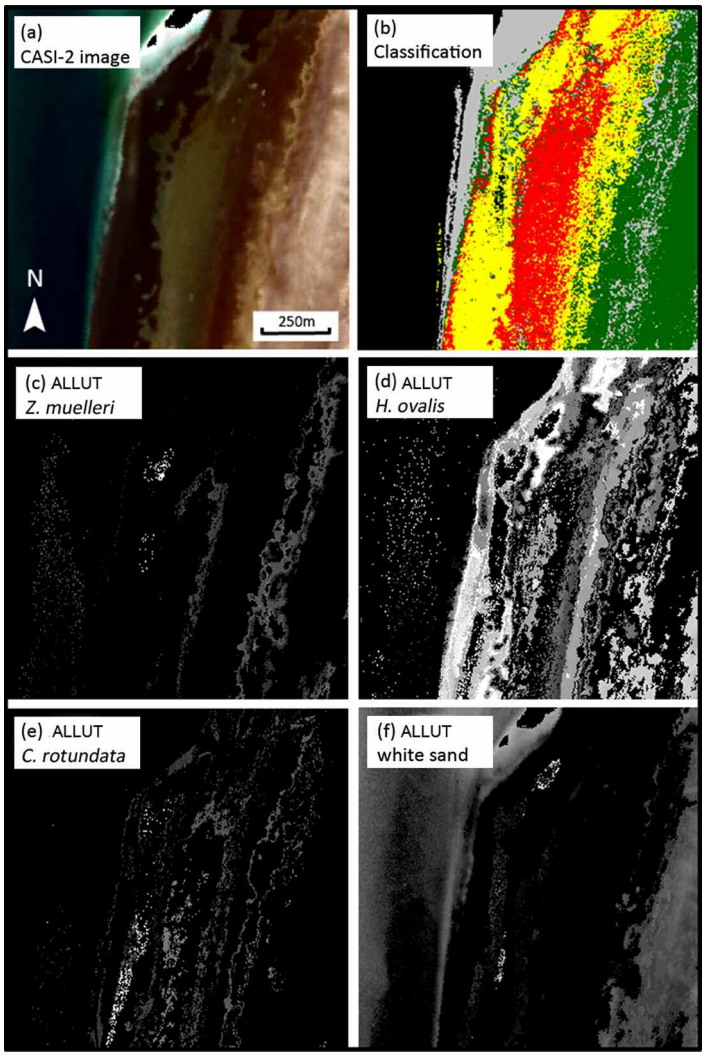

Fig. 10. Example images from the northeastern section of the Moreton Bay-Rainbow Channel CASI-2 image, in an area with pronounced depth variation and mono-specific patches of several types of seagrass. (a) True color red-green-blue image; (b) independent classification used for the accuracy assessment: yellow – *Cymodocea rotundata*; red – *Syringodium isoetofolium*; dark green – *Zostera muelleri*; gray – sand; black – deepwater/unmapped; (c) - (f) endmember fraction images derived from the ALLUT method for (c) *Zostera muelleri*, (d) *Halophila ovalis*, (e) *Cymodocea rotundata*, and (f) white sand. Note that (b) uses different classes than the inversion methods (see text for detail).

Findings from the retrieved to in-situ R_b comparisons (Fig. 9) and accuracy assessment for MB classifications (Fig. 10) indicated that those inversions using more detailed representations of the environmental features contributing to R_b, i.e., allowing more benthic features to make up a pixel, more accurately retrieved the R_b shape, producing more accurate benthic-substrate cover classifications. ALLUT, CRISTAL, and BRUCE allowed more detailed representations of benthic features making up a pixel to estimate R_b values, whereas SAMBUCA was limited to a set of three possible components, and HOPE does not produce an output R_b image. Image-based factors contributing to the pixel value, including atmospheric noise, water-surface attributes (e.g., glint), and large variations in water column properties may also have affected retrieved R_b values. The latter point stresses the need for effective atmospheric and air-water interface corrections to retrieve reliable R_b values.

Processing and parameterization

Significant differences between the inversion methods were recorded for the time each took to process the LSI and MB scenes (Table 5), with the differences being due to the complexity of the inversion method used, number of parameters, how the equation and its solution were written in code, and the software environment used to implement the code. The processing speeds or efficiencies for each method and scene reflect the design of these inversion methods: the HOPE and CRISTAL were the fastest, followed by ALLUT, BRUCE, and SAMBUCA. These relative differences in processing speeds mainly reflect the cost for increased detail and complexity in the SA or LUT inversion and the number of parameters used, e.g., contrasts HOPE, BRUCE, and ALLUT's parameters (Table 3), and may also reflect inefficient coding of the RTE inversion methods. For some algorithms, such as SAMBUCA, a large

number of additional parameters are calculated for each pixel to provide more quantitative information on the accuracy and validity of retrieved bathymetry, substratum visibility, IOP, and the R_b values, including signal-to-noise estimates. The code types and processing environments may not be optimum for speed or accuracy for each method. Where required, each of these codes can now be improved with the knowledge gained during this comparison exercise.

Discussion

Understanding the current status of optically shallow water mapping to advance this area of research and implementation

The assessment presented in the last section provides key points about how this set of approaches for mapping depth, water quality, and benthic/substrate information from hyperspectral airborne data perform relative to a reference data set and to one another. These assessments identify a continuum of methods, ordered by number of input parameters, complexity and duration of processing algorithm and environment, and accuracy/robustness of output. Limitations of each method were also established; highlighting areas where future work is required to further test and refine the algorithms.

No previous studies have provided an intercomparison of the empirical and semi-analytical inversion methods for mapping depth, water quality, and benthic/substrate information. Empirical approaches, such as those used by Lyzenga (1981), for estimating depth are mostly limited to optically shallow waters where uniformly clear water bodies over the same benthos/substrate occur. A confirmation and extension to previously published work was that the SA and LUT inversion methods were more robust and accurate than the empirical approach over a range of depths, water clarities, and benthos/substrate types, and that they can be implemented in relatively simple form with limited parameters (hence limited need for local data), or in more complex forms, requiring more locally specific input parameters. The approaches presented here form a continuum from empirical to SA and LUT with increasing levels of detail in terms of input parameters. Potential users of these approaches can use our results to select the approach suited to their information requirements, type of environment, type of image data; type of field data, hardware/software capabilities, and personnel expertise. A tentative listing of approaches from simple to complex is (Lyzenga 1981) HOPE, CRISTAL, BRUCE, SAMBUCA, and ALLUT.

The accuracy and computational efficiency of each inversion method was limited by the complexity of the RTE or its inversion equation used, level of simplification in the input parameters, and the software environment in which the models are run. A number of papers have been published examining the effects of these factors on individual SA and LUT inversion methods, as outlined in the "*Introduction*" and "*Materials and methods*." By presenting the results of each method together, the relative effects of these differences become apparent, especially in relation to the number and type of IOP spectra, R_b endmembers, and the methods used to mix R_b endmembers. Several image correction processes are likely to have affected the accuracy of retrieved depth, water quality, and benthic reflectance, and could not be assessed systematically in this work. We acknowledge they may have affected the accuracy of our results and require further investigation: atmospheric correction, geometric correction, air-water interface corrections, and collection of spatial-temporal matched IOP and benthic feature and reflectance data.

Implications for future optical shallow water mapping applications

Two critical implications for future application of optically shallow water mapping algorithms were identified, relating to a specification for best practice approaches and outstanding uncertainties about each of the SA and LUT inversion methods.

In terms of "best practice" for selecting algorithms to map bathymetry, water quality and benthic/substrate information in optically shallow coastal waters, there is no set list of best to worst, as an optimal method also depends on type of environment to be mapped; range of depths; range of water clarities; number and type of benthic/substrate features; image type; field data types and extent; available hardware and software; and personnel with processing expertise. Potential users of bathymetry, water quality, and benthic/substrate information in optically shallow coastal waters, including scientists, resource managers, and defense agencies all have different sets of constraints within the variables listed above. Our assessment shows that all of the SA and LUT inversion methods provided relatively accurate data at varying levels of processing speed and with varying amounts of supporting information. Several of the approaches can be run very quickly on applications where limited field data on bathymetry, IOP values and R_b spectra are present – HOPE and CRISTAL. LUT-based approaches do need more time in parameterizing and creating the Look-Up Tables. However, more accurate and robust results are provided by using more locally specific data on IOPs and R_b spectra, and allowing more complexity and error checking in the SA and LUT inversion methods, e.g., BRUCE, SAMBUCA, and ALLUT. If an aquatic environment contains both optically deep water, due to increased turbidity or depth, and optically shallow water, an ideal inversion method needs to incorporate a method for assessing per pixel whether there is a measurable water leaving radiance or reflectance signal from the substratum. This will prevent random estimations of bathymetry and substrate composition by ensuring the spectral information in the water leaving radiance or reflectance is sufficient for resolving the desired range of benthic variables.

A number of questions still remain concerning the absolute accuracy and performance of the inversion methods, especially in relation to their ability to be applied in operational, large area mapping, and monitoring capacities from satellite hyperspectral image data. This assessment only covered airborne hyperspectral image data from two different coastal

sites in the Pacific Ocean and Caribbean Sea, and provides a guide for future intercomparisons, which should be conducted as a priority on (1) additional sites with similar airborne and fully matched field data sets, but variable depth and water clarities; and (2) the same or additional sites with operational satellite hyperspectral image data. These additional intercomparisons would allow complete assessment of IOP and R_b spectra retrieval accuracies, and also show if the algorithms can be applied in simple and more complex forms across a large number of sites.

On a separate, but related issue, coastal environments around the world typically experience significant variations in water clarities and consequent visibility to the substratum. For bathymetry and substratum mapping, the approaches covered here only deal with optically shallow areas, which cannot be used in for mapping bathymetry and substratum reflectance in optically deep waters. Passive and active (e.g., side-scan sonar, multi-beam, etc.) mapping approaches for these areas exist but are usually boat based and can therefore not be used in shallow waters (<5.0 m deep). Airborne laser depth sounding operates in approximately the same range as the optical and nearby infrared methods discussed here. Airborne and spaceborne hyperspectral imagery perform well in the shallowest waters till they are optically deep. Thus, a complementarity exists between these methods when large coastal or coral reef areas need systematic mapping.

Comments and recommendations

Our intercomparison of the most commonly used empirical and semi-analytic and look-up table inversion methods for mapping bathymetry, water column IOP, and benthic/substrate reflectance provided either absolute or relative assessments of the accuracy of the retrieved parameters, the time taken to complete the processing and the main attributes of each method, which controlled their accuracy and processing time. Absolute accuracy assessment was only possible with retrieved depths, various forms of relative accuracy assessment were used for other parameters. The results provide a unique test of state of the art shallow water mapping algorithms using hyperspectral image data and field data from two sites. The assessment results showed:

1. Accuracy and processing time of each mapping algorithm: The semi-analytic methods were more accurate than the empirical approach of Lyzenga (1978), and the accuracy and processing times were inversely related to the complexity of the models used, with the simplest models, requiring least input data, but being the quickest with lower accuracies.
2. Conditions under which existing mapping models do and don't work: All SA and LUT inversion methods provided moderately accurate retrievals of bathymetry, water column IOP, and benthic/substrate reflectance within optically shallow areas, < 10m depth, with relatively homogenous benthic/substrate cover types. More accurate retrievals were obtained from the more complex and locally parameterized methods. Several algorithms incorrectly retrieved substratum parameters in optically deep waters (where there is no measureable signal from the substratum).
3. The adaptability of mapping models to two different locations and two imaging sensors: This was only able to be assessed in a limited context, between two sites and two airborne hyper-spectral sensors (PHILLS, CASI-2). Each SA and LUT inversion model performed well across the two sites, although there were marked differences in performance of each model between the sites.
4. Recommended products and procedures for mapping in optically shallow waters: Due to the number of variables that control the nature of spatial information required on bathymetry, water column IOP, and benthic/substrate reflectance within optically shallow areas, no single method or data set can be considered optimal. These mapping applications fall in between two extremes: (i) mapping where access and in-situ data are not possible; and (ii) full access to a site with collection of bathymetry, water column IOP, and benthic/substrate reflectance coincident with image data collection. Our assessment shows that the simpler, highly efficient algorithms, such as HOPE and CRISTAL, suit the first type of application, while SAMBUCA, BRUCE, and ALLUT, which are more complex and require local data and take longer to process are at the other extreme. A recommended approach is to work within the limits of the image, field data, and processing capabilities of the coastal environment and group conducting the mapping work, as outlined in the sections above. For example, limited bathymetric, water column IOP, and benthic/substrate reflectance data and image-processing ability could use the Lyzenga (1978) approach or HOPE to estimate bathymetry in environments with homogeneous substrate/benthos and within the known depth limits of the algorithms. Identification of depth limits is critical, and it is essential that advanced inversion methods can identify these nonoptically shallow waters on a per pixel basis to avoid erroneous bathymetry and substratum mapping.
5. International best science practice: Each of the SA and LUT inversion methods has advantages and disadvantages. Best practice would be to be as pragmatic as possible in terms of selecting a processing technique to match the environmental variable to be mapped, along with available image and field data and processing expertise, and ensure that this is done within known bounds (e.g., depth limits) of the image and algorithm combination. An ideal algorithm would synthesize the advantages of each approach outlined above into one approach that will deliver accurate bathymetry, water column optical properties, and substratum composition, in an efficient programming environment with as many as possible relevant quality control procedures built in. This approach should also deal with

optically shallow to optically deep waters explicitly and be able to work with sub-optimal earth observation data, as will often be the case when applied operationally. A re-analysis of these same or additional sites with satellite hyperspectral image data with lower spatial and radiometric resolution would be instructive to establish if these techniques can be applied over a the global range of coastal environments.

List of Acronyms

ALLUT: Adaptive Linearized Look-up Trees (s)

BRUCE: The Bottom Reflectance Un-mixing Computation of the Environment model

CASI-2: Compact Airborne Spectrographic Imager type 2

CDOM: Chromophoric (or Coloured) dissolved organic matter

CRISTAL: The Spectrum-Matching and Look-up-Table inversion method

HOPE: Hyperspectral Optimization Process Examplar model

IOP: Inherent optical property

LSQ: Least squares minimum

LSI: Lee Stocking Island Horseshoe Reef(Bahama's)

LUT: Look up table

MB: Moreton Bay Rainbow Channel

NAP: Non algal particulate matter

SAMBUCA: Semi-Analytical Model for Bathymetry, Un-mixing, and Concentration Assessment

SDI: Substratum Detectability Index

SIOP: Specific inherent optical property

TAFKAA: The algorithm formerly known as ATREM (ATmospheric REMoval)

WOMBAT: coastal Waters and Ocean MODTRAN-4 Based Atmospheric correction"

List of Symbols

R_{rs}: Remote-sensing reflectance (above surface L_u/E_d)

$R_{rs}^{SGC}(\lambda)$: Sunglint-corrected R_{rs}.

R(0-): Subsurface irradiance reflectance

r_{rs}: Sub-surface remote-sensing reflectance, or ratio of the upwelling radiance to downwelling irradiance evaluated just below the surface

r_{rs}^{dp}: Remote-sensing reflectance for optically deep waters

$r_{rs}^{\mathrm{dp\_model}}$: Modeled remote-sensing reflectance for optically deep waters

r_{rs}^{model}: Modeled remote-sensing reflectance for an optical shallow water body

ρ(λ): Benthic spectral reflectance

NEΔr_{rsE}: Noise equivalent difference in reflectance (Wettle et al. 2004)

Δ: Optimization residuum

$w(\lambda_i)$: Spectral band weighting factor

α[sr^{-1}]: Spectral angle between reference spectra and the spectra of the pixel in question as defined in the Spectral Angle Mapper (SAM, Kruse et al. 1993)

$a(\lambda)$: Absorption coefficient

$a_{phy}^{*}(\lambda)$: Chlorophyll-a specific absorption spectrum

a_{phy}: phytoplankton pigments absorption spectrum

$a_{\mathrm{NAP}}^{*}(\lambda_0)$: NAP specific absorption at reference wavelength

a_{NAP}: NAP absorption spectrum

a_w: Absorption coefficient of pure water

P: $a_\phi(440)$, the variable for phytoplankton absorption coefficient at 440 nm

a_g: Absorption coefficient for gelbstoff and detritus (Carder et al. 1999)

a_{CDOM} (440 nm): CDOM absorption coefficient at 440 nm

$a_{\mathrm{CDOM}}^{*}(\lambda_0)$: CDOM absorption normalized at $_{-0}$

G: Is $a_g(440)$ = gelbstoff and detritus absorption at 440 nm

S: Spectral slope of a_g

S_{CDOM}: Spectral slope for CDOM absorption coefficient

S_{NAP}: Spectral slope for NAP absorption coefficient;

a_j^{*}: Specific inherent optical absorption properties (SIOPs) of j^{th} constituent with concentration C_j

B: Scattering coefficient

B_p: Particle backscattering coefficient (b_b:b)

$b_b(\lambda)$: Backscattering coefficient

b_{bw}: Backscattering coefficient of pure seawater

b_{bp}: Backscattering coefficient of suspended particles

X: $b_{bp}(550)$ backscattering coefficient of suspended particles at 550 nm

Y: The spectral shape parameter of particle backscattering

b_{bj}^{*}: Specific inherent optical backscattering properties (SIOPs) of j^{th} constituent with concentration C_j

$b_{bphy}^{*}(\lambda_0)$: Specific backscattering of algal particles at the reference wavelength of 542 nm

Y_{phy}: Power law exponent for the algal particles backscattering coefficient

$b_{b\mathrm{NAP}}^{*}(\lambda_0)$: Specific backscattering of NAP at the reference wavelength of 542 nm

$\rho_i(\lambda)$ and $\rho_j(\lambda)$: Spectral benthic reflectances of substratum i and j

B_i and B_j: Fractional cover of substratum i and substratum j within each pixel

ρ_{sand}^{+}: Spectrally normalized sand spectral reflectance

ρ_{grass}^{+}: Spectrally normalized grass spectral reflectance

$\rho sed_i(\lambda)$: Measured sediment reflectance spectral end member

$\rho veg_i(\lambda)$: Measured vegetation reflectance spectral end member

$\rho cor_i(\lambda)$: Measured coral reflectance spectral end member

B_{sed_i}: Fractional weighting coefficient of sediment bottom reflectance spectra

B_{veg_i}: Fractional weighting coefficient of vegetation bottom reflectance spectra

B_{cor_i}: Fractional weighting coefficient of coral bottom reflectance spectra

ρ^+: The 550 nm normalized spectral shapes of a specific bottom type

q_{ij}: Fractional cover of substratum i and substratum j within each pixel

B: Benthic reflectance value at 550 nm

H: Bottom depth

θ_w: Sub-surface solar zenith angle

θ_v: Sub-surface viewing angle from nadir

φ: Viewing azimuth angle from the solar plan

$D^C{}_u$: Optical path-elongation factor for photons from the water column

$D^B{}_u$: Optical path-elongation factor for photons from the bottom

Q: Subsurface upwelling irradiance to upwelling radiance conversion factor = is taken to be 4

C_{CHL}: Concentration of Chlorophyll *a*

C_{NAP}: Concentration of NAP

C_{CDOM}: Absorption of CDOM at 440 nm

Y_{phy}: Power law exponent for the algal particles backscattering coefficient

Y_{NAP}: Power law exponent for NAP backscattering coefficient

References

Adler-Golden, S. M., P. K. Acharya, A. Berk, M. W. Matthew, and D. Gorodetzky. 2005. Remote bathymetry of the littoral zone from AVIRIS, LASH, and QuickBird Imagery. IEEE Trans. Geosci. Remote Sens. 43:337-347 [doi:10.1109/TGRS.2004.841246].

Blondeau-Patissier, D., V. E. Brando, K. Oubelkheir, A. G. Dekker, L. A. Clementson, and P. Daniel. 2009. Bio-optical variability of the absorption and scattering properties of the Queensland inshore and reef waters, Australia. J. Geophys. Res. 114 C05003, [doi:10.1029/2008JC005039].

Boss, E., and J. R. V. Zaneveld. 2003. The effect of bottom substrate on inherent optical properties: Evidence of biogeochemical processes. Limnol. Oceanogr. 48:346-354 [doi:10.4319/lo.2003.48.1_part_2.0346].

Brando, V. E., and A. G. Dekker. 2003. Satellite hyperspectral remote sensing for estimating estuarine and coastal water quality. IEEE Trans. Geosci. Rem. Sens. 41:1378-1387 [doi:10.1109/TGRS.2003.812907].

———, J. M. Anstee, M. Wettle, A. G. Dekker, S. R. Phinn, and C. Roelfsema. 2009. A physics based retrieval and quality assessment of bathymetry from suboptimal hyperspectral data. Rem. Sens. Environ. 113:755-770 [doi:10.1016/j.rse.2008.12.003].

Bricaud, A., A. Morel, and L. Prieur. 1981. Absorption by dissolved organic matter of the sea (yellow substance) in the UV and visible domains. Limnol. Oceanogr. 26:43-53 [doi:10.4319/lo.1981.26.1.0043].

Carder, K. L., F. R. Chen, Z. P. Lee, and S. K. Hawes. 1999. Semi-analytic moderate resolution imaging spectrometer algorithms for chlorophyll a and absorption with bio-optical domains based on nitrate-depletion temperatures. J. Geophys. Res. 104:5403-5421 [doi:10.1029/1998JC900082].

Clark, R. K., T. H. Fay, and C. L. Walker. 1987. Bathymetry calculations with Landsat 4 TM imagery under a generalized ratio assumption. Appl. Opt. 26:4036–4038 [doi:10.1364/AO.26.4036_1].

Decho, A. W., and others. 2003. Sediment properties influencing upwelling spectral reflectance signatures: The "biofilm gel effect." Limnol. Oceanogr. 48:431-443 [doi:10.4319/lo.2003.48.1_part_2.0431].

Dekker, A. G., R. Mount, and A. Jordan. 2007. Satellite and airborne imagery including aerial photography for benthic habitat mapping, p. 11-28. Marine benthic habitat mapping special publication. Geological Association of Canada: 327 p. ISBN-13: 978-1-897095-33-1

Dierssen, H. M., R. C. Zimmerman, R. A. Leathers, T. V. Downes, and C. O. Davis. 2003. Ocean color remote sensing of seagrass and bathymetry in the Bahamas Banks by high resolution airborne imagery. Limnol. Oceanogr. 48:444-455 [doi:10.4319/lo.2003.48.1_part_2.0444].

———, R. M. Kudela, J. P. Ryan, and R. C. Zimmerman. 2006. Red and black tides: Quantitative analysis of water-leaving radiance and perceived color for phytoplankton, colored dissolved organic matter, and suspended sediments. Limnol. Oceanogr. 51:2646-2659 [doi:10.4319/lo.2006.51.6.2646].

Giardino, C., V. E. Brando, A. G. Dekker, N. Strömbeck, and G. Candiani. 2007. Assessment of water quality in Lake Garda (Italy) using Hyperion. Rem. Sens. Environ. 109:183-195 [doi:10.1016/j.rse.2006.12.017].

Goodman, J., and S. L. Ustin. 2007. Classification of benthic composition in a coral reef environment using spectral unmixing. J. Appl. Rem. Sens. 1:011501 [doi:10.1117/1.2815907].

Green, E. P., P. J. Mumby, A. J. Edwards, and C. D. Clark. 2000. Remote sensing handbook for tropical coastal management. UNESCO.

Hedley, J., C. Roelfsema, and S. R. Phinn. 2009. Efficient radiative transfer model inversion for remote sensing applications. Rem. Sens. Environ. 113:2527-2532 [doi:10.1016/j.rse.2009.07.008].

IOCCG. 2006. Remote sensing of inherent optical properties: fundamentals, tests of algorithms, and applications.

IOCCG.

Klonowski, W. M., P. R. C. S. Fearns, and M. J. Lynch. 2007. Retrieving key benthic cover types and bathymetry from hyperspectral imagery. J. Appl. Rem. Sens. 1:011505 [doi:10.1117/1.2816113].

Kruse, F. A., and others. 1993. The spectral image processing system (SIPS)—Interactive visualization and analysis of imaging spectrometer data. Remote Sens. Environ. 44:145-163 [doi:10.1016/0034-4257(93)90013-N].

Lee, Z., K. L. Carder, S. K. Hawes, R. G. Steward, T. G. Peacock, and C. O. Davis. 1994. Model for the interpretation of hyperspectral remote-sensing reflectance. Appl. Optics 33:5721-5732 [doi:10.1364/AO.33.005721].

———, K. L. Carder, C. D. Mobley, R. G. Steward, and J. F. Patch. 1999. Hyperspectral remote sensing for shallow waters: II. deriving bottom depths and water properties by optimization. Appl. Optics 38:3831-3843 [doi:10.1364/AO.38.003831].

———, L. C. Kendall, R. F. Chen, and T. G. Peacock. 2001. Properties of the water column and bottom derived from Airborne Visible Imaging Spectrometer (AVIRIS) data. J. Geophys. Res. 106:11639-11651.

Lee, Z. P., K. L. Carder, C. D. Mobley, R. G. Steward, and J. S. Patch. 1998a. Hyperspectral remote sensing for shallow waters. I. A semianalytical model. Appl. Opt. 37:6329-6338 [doi:10.1364/AO.37.006329].

———, ———, R. G. Steward, T. G. Peacock, C. O. Davis, and J. S. Patch. 1998b. An empirical algorithm for light absorption by ocean water. J. Geophys. Res. 103:27967-927978.

Lesser, M., and C. Mobley. 2007. Bathymetry, water optical properties, and benthic classification of coral reefs using hyperspectral remote sensing imagery. Coral Reefs 26:819-829 [doi:10.1007/s00338-007-0271-5].

Lim, A., J. D. Hedley, E. Ledrew, P. J. Mumby, and C. Roelfsema. 2009. The effects of ecologically determined spatial complexity on the classification accuracy of simulated coral reef images. Rem. Sens. Environ. 113:965-978 [doi:10.1016/j.rse.2009.01.011].

Louchard, E. M., R. P. Reid, F. C. Stephens, C. O. Davis, R. A. Leathers, and T. V. Downes. 2003. Optical remote sensing of benthic habitats and bathymetry in coastal environments at Lee Stocking Island, Bahamas: A comparative spectral classification approach. Limnol. Oceanogr. 48:511-521 [doi:10.4319/lo.2003.48.1_part_2.0511].

Lyzenga, D. R. 1978. Passive remote sensing techniques for mapping water depth and bottom features. Appl. Optics 17:379-383 [doi:10.1364/AO.17.000379].

———. 1981. Remote sensing of bottom reflectance and water attenuation parameters in shallow water using aircraft and Landsat data. Inter. J. Rem. Sens. 1:71-82.

Marshall, B. R., and R. C. Smith. 1990. Raman scattering and in-water ocean optical properties. Appl. Opt. 29:71-84 [doi:10.1364/AO.29.000071].

Mcintyre, M. L., D. F. Naar, K. L. Carder, B. T. Donahue, and D. J. Mallinson. 2006. Coastal bathymetry from hyperspectral remote sensing data: comparisons with high resolution multibeam bathymetry. Mar. Geophys. Res. 27:128-136 [doi:10.1007/s11001-005-0266-y].

Mobley, C. D. 1994. Light and water: Radiative transfer in natural waters. Academic Press.

———, and others. 1993. Comparison of numerical models for computing underwater light fields. Appl. Opt. 32:7484-7504 [doi:10.1364/AO.32.007484].

——— and others. 2005. Interpretation of hyperspectral remote-sensing imagery by spectrum matching and look-up tables. Appl. Opt. 44:3576-3592 [doi:10.1364/AO.44.003576].

———, and W.P. Bissett. 2011. CRISTAL user's guide and technical documentation. *In* Sequoia Scientific, Inc., Bellevue, WA, USA. pp 105.

Morel, A. 1974. Optical properties of pure water and pure sea water, p. 1-24. *In* N. G. Jerlov and E. S. Nielsen [eds.], Optical aspects of oceanography. Academic Press.

O'Neill, N. T. O., Y. Gauthier, E. Lambert, L. Hubert, J. M. M. Dubois, and H. R. Edel. 1988. Imaging spectrometry applied to the remote sensing of submerged seaweed, p. 315-318. *In* T. D. G. a. J. J. Hunt [ed.], 4th Int. Coll. on spectral signatures of objects in remote sensing. ESA.

Oubelkheir, K., and others. 2006. Using inherent optical properties to investigate biogeochemical dynamics in a tropical macrotidal coastal system. J. Geophys. Res. (C Oceans) 111, C07021 :pp 15.

Philpot, W. D. 1989. Bathymetric mapping with passive multispectral imagery. Appl.Opt. 28:1569-1578 [doi:10.1364/AO.28.001569].

Phinn, S., and others. 2005. An integrated remote sensing approach for adaptive management of complex coastal waters. Final report-Moreton Bay remote sensing tasks., p. 124. *In* S. R. Phinn and A. Dekker [eds.]. CSIRO Land & Water.

———, C. Roelfsma, V. E. Brando, A. Dekker, and J. M. Anstee. 2006. Remote sensing for coastal ecosystem indicators assessment & monitoring (SR), p. 117. Coastal CRC Technical Report. CRC for Coastal Zone, Estuary and Waterway Management, Indooroopilly, Qld, Australia..

———, C. Roelfsema, A. Dekker, V. Brando, and J. Anstee. 2008. Mapping seagrass species, cover and biomass in shallow waters: An assessment of satellite multi-spectral and airborne hyper-spectral imaging systems in Moreton Bay (Australia). Rem. Sens. Environ. 112:3413-3425 [doi:10.1016/j.rse.2007.09.017].

Polcyn, F. C., W.L. Brown, and I. J. Sattinger. 1970. The measurement of water depth by remote sensing techniques. Institute of Science and Technology, Report 897326-F, Willow Run Laboratories, U. of Michigan, Ann Arbor, 1970.

Pope, R. M., and E. S. Fry. 1997. Absorption spectrum (380-700 nm) of pure water. II. Integrating cavity measurements. Appl. Opt. 36:8710-8723 [doi:10.1364/AO.36.008710].

Qin, Y., A. G. Dekker, V. E. Brando, and D. Blondeau-Patissier. 2007. Validity of SeaDAS water constituents retrieval algorithms in Australian tropical coastal waters. Geophys. Res. Letters 34 L21603, pp 4. [doi:10.1029/2007GL030599].

Roelfsema, C., S. R. Phinn, W. C. Dennison, A. G. Dekker and V. E. Brando. 2002. Monitoring cyanobacterial blooms of Lyngbya Majuscula in Moreton Bay, Australia by combining field techniques with remote sensing. *In*: Proceedings of the 11th Australasian Remote Sensing and Photogrammetry Conference, Brisbane, 2-6 September, CD-Rom, Causal Publications.

———, ———, ———, ———, and ———. 2006. Monitoring toxic cyanobacteria *Lyngbya majuscula* (Gomont) in Moreton Bay, Australia by integrating satellite image data and field mapping. Harmful Algae 5:45-56 [doi:10.1016/j.hal.2005.05.001].

Stephens, F. C., E. M. Louchard, R. P. Reid, and R. A. Maffione. 2003. Effects of microalgal communities on reflectance spectra of carbonate sediments in subtidal optically shallow marine environments. Limnol. Oceanogr. 48:535-546 [doi:10.4319/lo.2003.48.1_part_2.0535].

Strang, G. 1988. Linear algebra and its applications. Wellesley-Cambridge Press (Wellesley, MA), USA.

Stumpf, R. P. 1987. Remote sensing of suspended sediments in estuaries using atmospheric and compositional corrections to AVHRR data, p. 205-222. 21st Symp. on Rem. Sens. of Environment.

Wettle, M., V. E. Brando, and A. G. Dekker. 2004. A methodology for retrieval of environmental noise equivalent spectra applied to four Hyperion scenes of the same tropical coral reef. Rem. Sens. Environ. 93:188-197 [doi:10.1016/j.rse.2004.07.014].

———, A. G. Dekker, and V. E. Brando. 2005. Monitoring bleaching of tropical coral reefs from space: A feasibility study using a physics-based remote sensing approach, Technical Report , CSIRO Wealth From Oceans Flagship, CSIRO, Canberra, Australia: pp 87.

Zaneveld, J. R. V., and E. Boss. 2003. The influence of bottom morphology on reflectance: Theory and two-dimensional geometry model. Limnol. Oceanogr. 48:374-379 [doi:10.4319/lo.2003.48.1_part_2.0374].

Zhang, H., K. J. Voss, R. P. Reid, and E. M. Louchard. 2003. Bidirectional reflectance measurements of sediments in the vicinity of Lee Stocking Island, Bahamas. Limnol. Oceanogr. 48:380-389 [doi:10.4319/lo.2003.48.1_part_2.0380].

Submitted 15 October 2010
Revised 21 June 2011
Accepted 29 June 2011